NICKEL OXIDE PASSIVATION PROCESSING FOR MICROSTRIP GAS CHAMBER DETECTOR

Mingzhe Lu

B. S., Nankai University, Tianjin, China, 1985

M. S., Nankai University, Tianjin, China, 1988

A THESIS SUBMITTED IN PARTIAL FULFILLMENT
OF THE REQUIREMENTS FOR THE DEGREE OF
MASTER OF APPLIED SCIENCE

in the School
of
Engineering Science

SIMON FRASER UNIVERSITY
July 1997

National Library
of Canada

Acquisitions and
Bibliographic Services

395 Wellington Street
Ottawa ON K1A 0N4
Canada

Bibliothèque nationale
du Canada

Acquisitions et
services bibliographiques

395, rue Wellington
Ottawa ON K1A 0N4
Canada

Your file Votre référence

Our file Notre référence

0-612-24187-4

Canada

APPROVAL

Name: Mingzhe Lu

Degree: Master of Applied Science

Title of Thesis: **Nickel Oxide Passivation Processing for Microstrip Gas Chamber Detector**

Examining Committee:

Chair
Senior Lecturer Susan Stevenson
Department of Engineering, Simon Fraser University

Supervisor
Asso. Prof. Glenn H. Chapman
Department of Engineering, Simon Fraser University

Asso. Prof. M. (Ash) Parameswaran, Simon Fraser Unive.
Department of Engineering, Simon Fraser University

Dr. Greg Stuart, Tantus Electronics Inc.

External examiner
Prof. Andrew Rawicz, Simon Fraser Unive.
Department of Engineering, Simon Fraser University

Date Approved: July 25, 1997

Abstract

Microstrip gas chambers (MSGC), as a position sensitive radiation detector, have attracted intensive attentions since they have been introduced in 1988. Due to their promising features such as good position resolution, excellent energy resolution, high rate capability and moderate cost, MSGCs have become one of the main components for particle tracking in high energy physics experiments and non destructive testing in other industrial and medical applications. It was clear from the beginning that several problems remained to be solved before wide spread use of the device. Among them, the charging up of the insulating substrate can cause the instabilities of the MSGC system operation.

Ion accumulation can be eliminated by decreasing the surface resistance of MSGC substrates to the $10^{12} \sim 10^{14}$ Ω/square, which is conductive enough to remove the charge, but resistive enough to maintain the high voltage between anodes and cathodes. In this thesis, a nickel oxide passivation technique is employed to achieve the desired sheet resistance. A thin layer of nickel oxide is deposited on the top of MSGC prints by DC sputtering deposition. It has been found that introducing oxygen into the sputtering chamber plays a critical role in the formation of the nickel oxide layer, and the desired sheet resistance can be achieved when the nickel atoms are mostly oxidized in a post baking process.

To understand and control the passivation process, we adopted several kinds of techniques to characterize the sputtering deposition and test the performance of the nickel oxide layer. A real time chromatic system, consisting of a color CCD camera and a computer, is used to monitor the color variation of plasma, which reflects the interaction between oxygen and nickel molecules. The measurement results show that the post baking process causes the nickel atoms to be oxidized by absorbing oxygen molecules externally. The capability of the nickel oxide layer to remove the accumulated ions is examined by simulating a high radiation rate with a scanning electron microscope.

A detailed description of the MSGC print fabrication, gas chamber system and the x-ray detection is provided in this thesis. With QPA02 preamplifier, we observed the output signal corresponding to the x-ray radiation from ^{55}Fe source. Additionally, two new approaches for microgap chamber print fabrication have also been proposed.

To my kids

Acknowledgments

I gratefully acknowledge the guidance and assistance of my supervisor Dr. Glenn Chapman. I would like to thank Dr. Greg Stuart of Tantus Electronics Corp. and Dr. Martin Salomon of TRIUMF for their valuable suggestions and comments.

I also received a lot of help from other faculty members, staff and graduate students of microelectronics group during this research. Mr. Bill Woods helped me a great deal with sputtering deposition and other fabrication processes. Mr. Henry Fu participated in part of this project. In addition, I am very thankful to Dr. Gary Leach, from Department of Chemistry at Simon Fraser University, for his help on chemical properties of gas, and to Mr. Kenneth Myrtle, from Department of Physics at Simon Fraser University, for his help on Auger spectroscopy measurement.

The work reported in this thesis is accomplished in Engineering Department, Simon Fraser University and financially supported by ASI, Tantus Electronics Corp. and Graduate Fellowship of Simon Fraser University.

CONTENTS

APPROVAL ii

ABSTRACT iii

ACKNOWLEDGMENT v

TABLE OF CONTENTS vi

LIST OF FIGURES x

LIST OF TABLES xiii

Chapter 1 Introduction 1

1.1 Operation of Microstrip Gas Chamber (MSGC) 2

1.1.1 Multiwire Proportional Counter (MWPC)
1.1.2 Microstrip Gas Chamber (MSGC)
1.1.3 Ion Accumulation Problem in MSGC

1.2 Scope of The Thesis 8

Chapter 2 Microstrip Gas Chamber Prints 10

2.1 Design of microstrip print 11
2.2 Charge accumulation in MSGC 14
- **2.2.1 Charge accumulation phenomenon**
- **2.2.2 Previous works and results**
    - *2.2.2.1 Backplane field shaping*
    - *2.2.2.2 Ion implantation*
    - *2.2.2.3 Electrical conductive substrate*
    - *2.2.2.4 Substrate coated with conductive layer*
- **2.2.3 Nickel oxide passivation**

2.3 Print fabrication process 21
- **2.3.1 Surface preparation**
- **2.3.2 Sputtering deposition.**
- **2.3.3 Patterning**
- **2.3.4 Passivation with nickel oxide film.**

2.4 Summary 26

Chapter 3 Microstrip Gas Chamber Detection System 27

3.1 Microstrip gas chamber 28

3.2 QPA02 Amplifier 33
- **3.2.1 Schematic of QPA02 amplifier**
- **3.2.2 Performance of QPA02 amplifier**
- **3.2.3 Performance of QPA02 amplifier connecting with the MSGC**

3.3 Observation of X-ray radiation signals 41

3.4 Summary 43

Chapter 4 Passivation of MSGC Prints with Nickel Oxide Film 44

4.1 Passivation process 45

4.1.1 Nickel Oxide Deposition
4.1.2 Surface resistivity measurement
4.1.3 Experimental results
    4.1.3.1 Nickel oxide deposition in the low oxygen ambient
    4.1.3.2 Nickel oxide deposition in the high oxygen ambient
    4.1.3.3 Post baking process

4.2 Testing of passivation film in gas chamber ...57

4.2.1 Temporal behavior of signal from MSGC
4.2.2 Signal amplitude vs. cathode voltage
4.2.3 Pulse amplitude Vs drift voltage
4.2.4 Temporal stability of MSGC
4.2.5 Discharge damage

4.3 Summary 66

Chapter 5 Characterization of Nickel Film and Deposition Process...........68

5.1 Testing the performance of passivation film with the Scanning Electron Microscope 69

5.1.1 Charging up in Scanning Electron Microscopy
5.1.2 Experimental procedure
5.1.3 Results
5.1.4 Summary

5.2 Control of nickel sputtering deposition with colormetric monitoring 76

5.2.1 Plasma and sputtering process
5.2.3 Camcorder measurement of plasma

5.2.4 Computer-Camera measurement of plasma
5.2.5 Summary

Chapter 6 Conclusions and Future Works 88

References 91

Appendix 1 93

Apendix 2 96

Figure List

Figure 1.1 Gas-filled x-ray detector 3

Figure 1.2 Schematic of multiple wire proportional counter (each wire with its own amplifier) 5

Figure 1.3 Microstrip gas chamber 6

Figure 2.1 The electrode structure of MSGC print 12

Figure 2.2 End shape of MSGC prints 13

Figure 2.3 Schematic of multiple pattern mask for MSGC print 13

Figure 2.4 Microstrip with backplane electrode 16

Figure 2.5 Photolithographic patterning process (a) glass substrate after RCA cleaning, (b) aluminum deposition, (c) photoresist coating, (d) photolithographic patterning, (e) aluminum etching, (f) photoresist striping 23

Figure 2.6 MSGC print passivated with nickel oxide layer 25

Figure 3.1 The cross section view of the microstrip gas chamber 27

Figure 3.2 The top view of the microstrip gas chamber 29

Figure 3.3 The diagram of the MSGC wiring 30

Figure 3.4 Experimental setup 31

Figure 3.5 QPA02 test circuit diagram 34

Figure 3.6 Equivalent input circuit 35

Figure 3.7 Curves of output amplitude vs. positive and negative input amplitude of QPA02 amplifier. (a) Vcc1 = 5.0V and Vcc2 = 4.1V, (b) Vcc1 = 5.5V and Vcc2 = 2.7V 36

Figure 3.8 Impulse response of QPA02 (a) for positive input, (b) for negative input 38

Figure 3.9 Oscillation status 39

Figure 3.10 Output vs. input curve of QPA02 connected to MSGC 41

Figure 3.11 Schematic of data collection system for x-ray detection 42

Figure 3.12 The typical pulse profile of x-ray signals 42

Figure 4.1 Post baking setup 47

Figure 4.2 Layout of anodes and cathodes in the microstrip print 48

Figure 4.3 I-V curves of nickel oxide film of different thickness (a) 5 nm, (b) 25 nm, and (c) 50 nm when argon and oxygen flow rate ratio was 5:1 51

Figure 4.4 I-V curves of MSGC prints with different nickel film thickness. (a) around 50 nm, (b) around 25 nm, (c) around 5 nm when argon and oxygen ratio is 1:1 53

Figure 4.5 Output response of MSGC operated with Ar/CO$_2$ gas when V_c = -700V and V_d = -2000V 58

Figure 4.6 Output response of MSGC operated with Ar/CO$_2$ gas when V_c = -630V and V_d = -1000V 59

Figure 4.7 Output response of MSGC operated with Ar/CO$_2$ gas when the load resistance of QPA02 is 1MΩ 60

Figure 4.8 Relation between output pulse height and cathode voltage when MSGC was operated with Ar/CO$_2$ gas 61

Figure 4.9 Relation between output peak height and cathode voltage when MSGC was operated with Ar/DME gas 62

Figure 4.10 Curve of output pulse height Vs drift voltage when MSGC was operated with Ar/CO_2 gas when Vc = -700V 63

Figure 4.11 Curve of output pulse height Vs drift voltage when MSGC is operated with Ar/DME gas when Vc = -700V 63

Figure 4.12 Variation of output peak height of MSGC over one day 65

Figure 4.13 Damage of MSGC print by discharge 66

Figure 5.1 SEM images of (a) uncoated and (b) coated MSGC prints 72

Figure 5.2 SEM images of the (a) uncoated and (b) coated MSGC prints after 30 seconds of electron scanning 74

Figure 5.3 Comparison of SEM image of the coated and uncoated MSGC print 75

Figure 5.4 Schematic diagram of the system for chromacity measurement 77

Figure 5.5 Images of the plasma glow under (a) pure argon (b) 5:1 argon/oxygen (c) 1:1 argon/oxygen 79

Figure 5.6 The plasma image set for the pure argon chamber under different illuminztion setting of the camera 82
(a)110,(b)120,(c)130,(d)140,(e)150,(f)160,(g)170,(h)180,(i)190,(j)200

Figure 5.7 The plasma image set for the 1:1 argon/oxygen chamber under different illuminztion setting of the camera 83
(a)110,(b)120,(c)130,(d)140,(e)150,(f)160,(g)170,(h)180,(i)190,(j)200

Figure 5.8 Sampling points on the image of plasma glow 86

Table List

Table 2.1 Measurement results of MSGC print dimensions 25

Table 4.1 Sheet resistance of nickel oxide films formed in the low oxygen gas ambient 52

Table 4.2 Sheet resistance of nickel oxide films formed in the high oxygen gas ambient 52

Table 4.3 Measurement of resistance after baking, average resistance is 9.9×10^{10} Ω/square 55

Table 4.4 Measurement of resistance 3 days after baking, average resistance is 1.16×10^{12}Ω/square 55

Table 4.5 Measurement of resistance 4 days after baking, average resistance is 6.9×10^{11}Ω/square 56

Table 4.6 Measurement of resistance 5 days after baking, average resistance is 6.7×10^{12}Ω/square 56

Table 4.7 Measurement of resistance 6 days after baking, average resistance is 5.2×10^{12}Ω/square 56

Table 4.8 Resistivity of nickel films after various post heating processes 56

Table 5.1 Experimental results of measurement of plasma glow 80

Table 5.2 Experimental data of plasma chromatic measurement of pure argon chamber 84

Table 5.3 Experimental data of plasma chromatic measurement of 1:1 argon/oxygen chamber 85

Table 5.4 Experimental results of the multiple point chromatic detection (pure argon chamber) 86

Table 5.5 Experimental results of the multiple point chromatic detection (1:1 argon/oxygen chamber) 86

Table 5.6 Ratio between the r/b listed in Table 5.4 and Table 5.5 87

Chapter 1 Introduction

X-ray radiation, conceived by Roentgen in 1895, is one of the most significant discoveries in the history of physics [1]. Based on their penetrating ability, X-rays have been widely applied in medical and industrial radiography to study internal structure and detect inner defects of opaque objects. For those non-destructive testing applications in more extensive areas, many efforts have been made on improvement of position sensitive x-ray detector.

There exist many kinds of x-ray detectors, such as the ionization chamber, the cloud chamber, Geiger-Muller counter, scintillation counter, semiconductor detector, multiwire and drift chambers [2]. Among them, semiconductor detectors and detectors based on multiwire chamber are able to be built as one or two dimensional detector arrays to acquire spatial information.

The subject of the research for this thesis is investigation of the microstrip gas chamber (MSGC) [3] prints with the aim of eliminating the ion accumulation problem using a passivation coating. Study of the MSGC print fabrication process is aimed at achievement of position sensitive x-ray detector of high spatial resolution (less than half millimeter) and high response speed (in the order of 10 MHz).

In this chapter, two position sensitive gas detectors, multiple wire proportional counter and microstrip gas chamber detector, are described. The ion accumulation problem of a MSGC is discussed. The scope of this thesis will then also be presented.

1.1 Operation of Microstrip Gas Chamber (MSGC)

X-rays can be detected with gas detectors by collecting (and sometimes amplifying) the ions and electrons generated when atoms of special gas (such as argon) are ionized following the absorption of an x-ray [4]. In gas detectors, an intense electric field is usually employed to collect electrons. Avalanche amplification can be induced by collision of free electrons with gas atoms when the electrons are accelerated to sufficient velocity that more than one electron are produced by such collision.

The essential features of the gas-filled x-ray detector are shown schematically in Figure 1.1 [5]. The ionization chamber consists of a gas contained between two electrodes with a gap between them. In measurement, a positive and a negative potential is applied to anode and cathode to form a drift field which accelerates the charges. The avalanche amplification occurs in the region near the anode, where electric field intensity is usually large by using a small anode wire radius. The anode collects the electrons and outputs an electric signal. The positive ions are drained by the grid. The resistors paralleling the voltage source function as voltage divider, to apply the desired voltages to anode, cathode and grid at same time. The resistor in series with the voltage source is used to limit the current through the anode and cathode, to protect electrodes from damage due to discharge.

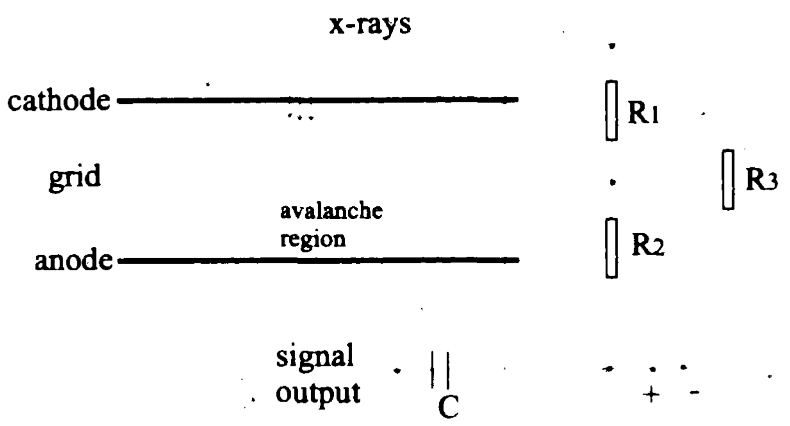

Figure 1.1 Gas-filled x-ray detector [5]

The relationship between the gas gain and the electric field intensity is [1]:

$$\alpha = APe^{-APV_i/E} = APe^{-BP/E} \qquad (1.1)$$

where P is the gas pressure, V_i is the gas ionization potential. A is a constant depending on the gas, $B = AV_i$. Usually the ionization coefficient is quoted as α / P in electrons per centimeter per torr. Values of A and B may be obtained from tabulated measurements [1].

Simple gas detectors, such as the Geiger counter, act as single detector for intensity measurement. But they are unable to work as an imaging device, to provide spatial information of x-ray radiation. Although a one or two dimensional array of separate x-ray detectors can be realized by combining many of such single detectors in a matrix arrangement, an integrated method was proposed by Charpak [6] to achieve a position sensitive x-ray detector in a single gas chamber by dividing electrodes into many strips. Based on this idea, the multiwire proportional counter detector was implemented, for which Charpak won the Nobel prize of Physics in 1992.

1.1.1 Multiwire Proportional Counter (MWPC)

To obtain spatial resolution, Charpak *et al* [6] constructed a chamber with multiple wire anodes, each wire with its own amplifier. As shown in Figure 1.2, an MWPC consists of a great number (~ 1000) of thin anode wires assembled in a plane to acquired spatial information. In detection, the electrons generated by radiation move toward anode wires driven by the drifting field between anode and cathode planes. Avalanche amplification occurs in the vicinity of anode wires, where the field strength is very high (over 10^3 V/mm). The spatial distribution of x-ray radiation can be determined by separately analyzing the output signals from each anode. However, it has been found that there are constraints on the response time and spatial resolution.

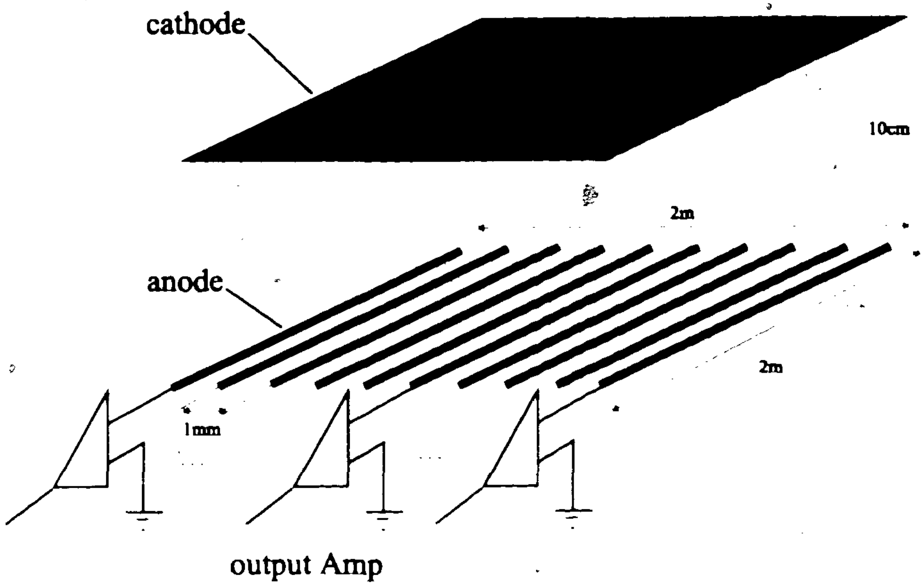

Figure 1.2 Schematic of multiple wire proportional counter (each wire with its own amplifier)

1.1.2 Microstrip Gas Chamber (MSGC)

A Microstrip Gas Chamber (MSGC), as shown in Figure 1.3, is an integrated thin film revision of the MWPC, proposed and implemented by Oed [3] in 1988. In a MSGC, thin film conductive strips deposited on an insulating substrate, rather than the floating wires in MWPC, are used to sense the spatial location of radiation. Those strips are placed alternatively as anodes and cathodes, and avalanche amplification usually occurs in the gap between the cathode and anode. Under this circumstance, the positive ions generated in the avalanche are drained by the cathodes, which is only in the order of a few hundred μm away from the anode. Consequently the drifting period is shortened substantially. Therefore, the MSGC is able to have a higher response speed up to MHz. Meanwhile, it is easy to achieve an anode pitch in the order of several tens of micrometers with IC fabrication technology. In addition, the structure of MSGC, in which the anodes are separated by cathodes, facilitates high field strengths, thereby maintaining high spatial resolution.

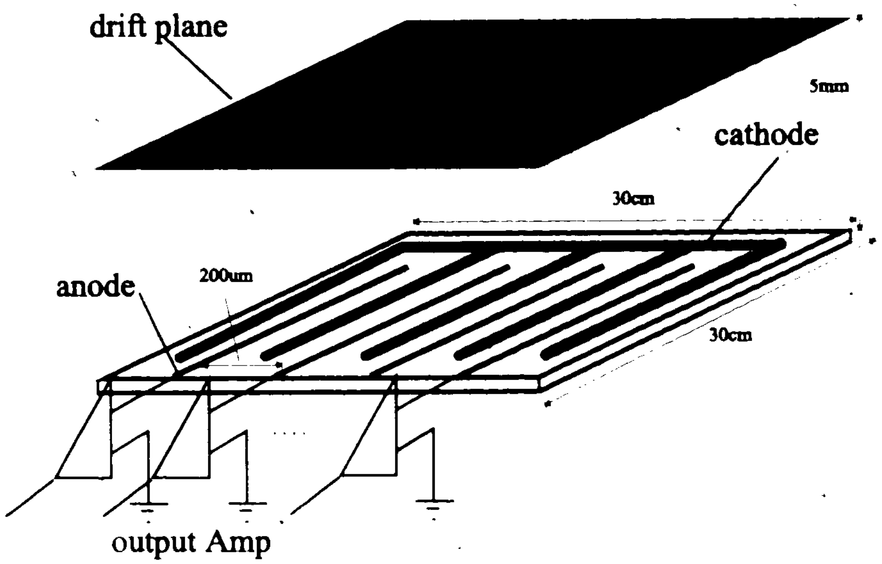

Figure 1.3 Microstrip gas chamber

1.1.3 Ion Accumulation Problem in MSGC

One major problem with an integrated MSGC is that the performance of the MSGC is highly affected by the ion accumulation on the insulating substrate [7]. As mentioned above, a cloud of positive ions moves towards the cathode strips during detection. If ions from the charge cloud reach the surface of the substrate, they may be trapped there because of their extremely reduced mobility on the insulator. Consequently, the surface of the substrate is charged until the applied electric field is completely compensated. Thus, over time, the efficiency of the detector will decline until at full compensation the microstrip plate device will cease to work.

Many efforts have been made to prevent charge accumulation on the surface of the MSGC print. Several approaches, such as back-plane electrode field shaping and conductive substrate methods, have been proposed and implemented [8]. The charge accumulation rate of the MSGC substrate is decreased if the bulk resistivity of the substrate is reduced [9] or if a layer of semi-insulating material is deposited on the substrate with the advantage of a reduced leakage current [10].

In both cases there is an important balance that must be maintained. The sheet conductivity in the areas between the electrodes must be low enough that it can prevent the charge accumulation. However, the film must also have a high enough resistance that it does not significantly disturb the voltage distribution between the anode and cathode. In particular it must remain stable at voltages of up to 700 V between electrodes with only 70 micron spacing between them. Previous researchers[10] have shown that this requires a sheet resistance between 10^{12} and 10^{14} Ω/square. Lower resistances will cause too much drain between the electrodes, while higher resistances will enable charge accumulation.

M. Salomon and G. Chapman et al proposed and implemented the passivation of MSGC prints with nickel oxide thin film [11]. This material was successfully deposited at TRIUMF. Subsequently also this film was successfully deposited on the MSGC prints fabricated in Simon Fraser University by DC sputtering, and achieved desired conductivity of nickel oxide film (10^{12} -10^{14} Ω/square). The MSGC prints passivated with nickel oxide film were also tested using a high x-ray radiation (equivalent to $0.7C/mm^2$) . The experimental results were satisfactory. However, duplicating the Nickel oxide with the required excess nickel content has proved difficult for other researchers. Pure Nickel Oxide is too resistive. It is necessary to start with a nickel film and add oxygen during the deposition processes to create a nickel rich nickel oxide. However finding and controlling the correct deposition parameters has proved difficult. Obviously, more comprehensive understanding of the nickel deposition process is essential before this passivation method can be accepted. The aim of this thesis is to establish repeatable deposition and other process parameters for creating the nickel oxide film of between 10^{12} and 10^{14} Ω/square. These films will be tested on prototype MSGC prints to create working detectors. However it is not the aim of the thesis to determine fully the characterization of these detectors with these films as that has been done by researchers previously[11].

1.2 Scope of The Thesis

Solving ion accumulation is important for the performance of a MSGC x-ray detector and is worthy of detailed investigation. The goal of this thesis is to study the passivation of MSGC prints on glass substrates with a nickel oxide layer. By taking advantage of the conductivity of the nickel oxide layer (in the range of 10^{13} ~10^{15} Ω/square), the charge accumulated on the surface of substrate can be removed. The nickel oxide film of desired resistivity has been achieved with sputtering deposition by introducing oxygen into sputtering chamber. To improve reproducibility and controllability of sputtering process, a color CCD imaging system was employed to monitor chromatic variation of plasma. The sheet resistivity and electric behavior of nickel oxide layer were measured with a semiconductor parameter analyzer. The stability of the electric properties of nickel oxide layer was observed as well. The ability to remove surface charge of nickel oxide layers has been examined by observing images of coated prints under exposure to electron flux in an scanning electron microscope (SEM).

The thesis was organized as following: in chapter 2, the existing methods solving the ion accumulation problem were presented. The advantages of the nickel oxide passivation were analyzed. The microstrip print was designed, and fabrication process was described. In chapter 3, the MSGC x-ray detection system was presented. The experimental results are also shown in this section. The passivation processing of MSGC prints is analyzed in chapter 4. Some measurement results were also shown in this chapter, including I-V curves. To test the performance of the nickel oxide film and control the deposition process, scanning electron microscopy and chromatic monitoring system are used, as presented in chapter 5. Chapter 6 is the conclusions and future works.

Chapter 2 Microstrip Gas Chamber Prints

In a gaseous chamber, x-ray radiation is detected based on avalanche amplification occurring in the region of an intensive electric field. Obviously, the performance of the detector is critically dependent on the gas mixture, sensing element geometry and fabrication process. Therefore, great effort should be taken on the design and fabrication of microstrip print.

In this section, the geometry of microstrip prints is proposed. We discuss the charge accumulation phenomenon in the MSGC. Previous works and testing results concerning charge accumulation is discussed. Finally, fabrication process of MSGC prints is presented.

2.1 Design of microstrip print

Before the microstrip print is designed the requirements of application and impact of print geometry on those aspects should be considered. For the investigations presented in this thesis, the following properties of an x-ray detector for real time imaging system were required: (a) fast response speed (over 1 MHz), *i.e.*, short charge collec~~tion~~ time; (b) high sensitivity, *i.e.*, large gain (in the order of 10^3); (c) good position accuracy (in submillimeter) and (d) high rate capacity (in the order of 10^6Hz/mm^2).

The avalanche gain of a MSGC is determined by the electric field distribution. The maximum gain is primarily limited by electric discharge, which can trip the high voltage between anode and cathode. Although high gain can be obtained by increasing electric field strength, the gas gain also depends on the dimensions of the avalanche region. It has already been observed that under the constant anode-cathode voltage, the gas gain increases due to the higher field strength around the anode strip as the anode-cathode gap is decreased. However, discharge will occur at lower gain for the MSGC of smaller anode-cathode gap. Therefore, the small anode-cathode gap also limits the achievable maximum gain of MSGC.

On the other hand, it is obvious that both the short charge collection time and good position accuracy require a narrow anode-cathode gap. In addition, the use of fast readout electronic requires the anode strip not be too resistive (i.e. very thin), but a wide anode will decrease electric field strength in the vicinity of anode strip, and cause the dramatic loss of avalanche gain. In earlier works [12, 13] it has already been pointed out that, the dominant mechanisms of discharge in the MSGC is most certainly a consequence of the ejection of electrons from the cathode either by field emission or by ion bombardment. Therefore, the width of cathode strips should also not be too small in a MSGC print.

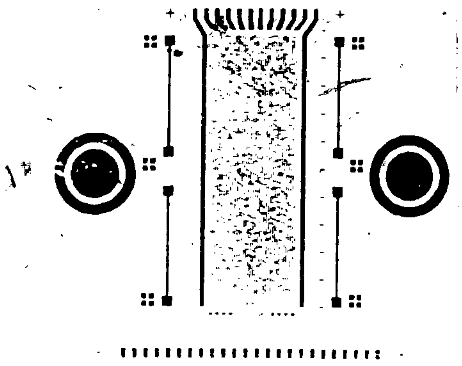

Figure 2.1 The electrode structure of MSGC print

A chromium mask of 400 μm anode pitc[illegible]as used to fabricate MSGC prints for the preliminary experiments. In this mask the widths of anode strips, cathode strips and anode-cathode gap are 20 μm, 90μm and 145μm, respectively. With an interdigital structure as shown in Figure 2.1, the electric field strength at the ends of the strips is substantially higher than at the parallel conductive sections. The possible potential difference was limited because of sparks at the ends. To avoid that, a structure shape presented in Figure 2.2 was chosen to keep the field strength at the parallel strip sections higher than at the remaining structure parts, and thus to obtain the highest possible gas amplification. With these kinds of end shapes, the discharge seldom occurs at the tips first in the high voltage testing.

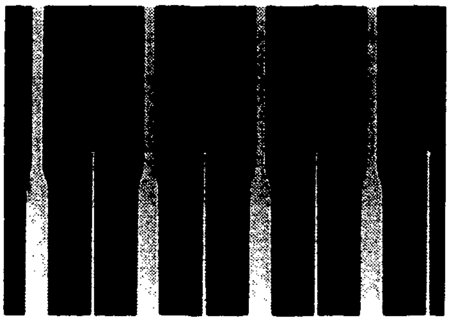

Figure 2.2 End shape of MSGC prints

Another mask for MSGC prints was designed at Simon Fraser University based on the concerns discussed previously. This mask was intended to investigate the requirements of a mask suitable for production of test prints for an imaging system. The following guidance were used to select main parameters of MSGC mask geometry: (a) keep the width of anode around 30 μm; (b) the width of cathode is not less than 60 μm and (c) the anode-cathode gap is in the range from 40 ~ 70 μm.

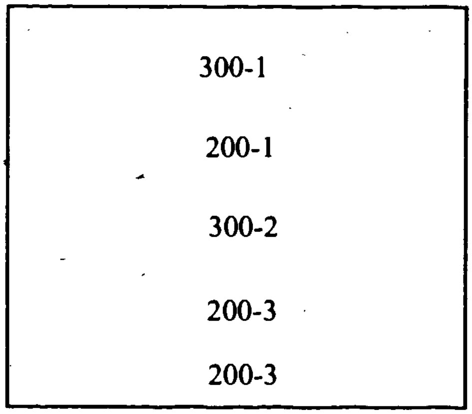

Figure 2.3 Schematic of multiple pattern mask for MSGC print

Figure 2.3 shows the mask designed at Simon Fraser University for use in a prototype imaging system. In one mask five microstrip structures were put in 7 cm × 7 cm square area, which is suitable for the size of glass substrates. A margin of 5 mm was reserved at the rim of the glass substrates for handling with a tweezers during the fabrication process. A cutting region of 3.8 mm in width was also reserved between every two patterns.

To diminish the electrical field at the ends of microstrips, round corners were used in all of those patterns. Two kinds of anode pitch, 200 μm and 300 μm, were used in this mask. For microstrips of 200 μm anode pitch three anodes are grouped together to achieve 600 μm equivalent pitch, while two anodes were grouped in the case of 300 μm pitch microstrips. Those patterns were labeled 200-3 and 300-2 in Figure 2.3, respectively. Single anode patterns with either 200 μm or 300 μm anode pitch, which are labeled as 200-1 and 300-1, respectively, were also incorporated in the mask.. The length of the anode strips for those four patterns was 1 cm. To observe the edge effects, a pattern of half-sized anodes was also put in the mask. The anode pitch of this pattern was 200 μm.

2.2 Charge accumulation in MSGC

2.2.1 Charge accumulation phenomenon

The insulating substrate makes it possible to realize the submillimeter electrode pitch in a MSGC, making the devices intrinsically capable of achieving high spatial resolution and fast response speed. On the other hand, the insulating substrate also causes ion accumulation problem in a MSGC, as mentioned in Chapter 1. Experimental observations have shown certain instabilities in the performance of MSGCs. MSGC prints fabricated on high resistivity substrate exhibit declines of gain during measurements at relatively moderate or high fluxes [14]. The gain variations can be categorized into short-term, reversible and reproducible changes, and long term gain modification, which leads to permanent degradation, and is accompanied by visible changes in the microstrip structure and surface.

Short-term gain drop can be observed in the exposed area. During the irradiation the gain decreases until reaching a plateau, or even totally ceasing to work. The steady-state gain value is dependent on the irradiation rate. This effect usually occurs in several minutes after the beginning of operation. This behavior is understood to be due to the charge accumulation on the insulating surface by positive ions generated in avalanching amplification.

Long term effects are explained as the contamination of MSGC print, such as polymerization or aging of materials due to exposure to x-ray radiation for a long period. They appear to depend on the choice of the substrate material, anode and cathode materials, working gases and other materials used in MSGC chamber.

2.2.2 Previous works and results

An impressive amount of works have been made to alleviate the charge accumulation problem since MSGC was proposed in 1988 [3] . Generally, methods used to prevent the charge accumulation can be categorized as following:

2.2.2.1 Backplane field shaping

The backplane method was employed by A. Oed when he implemented the first MSGC [3]. To prevent gas ions from accumulating on the surface of substrate, an another electrode was introduced on the rear side of microstrip substrate, as shown in Figure 2.4. The backplane electrode can be an evaporated metallic layer or a thin metal foil just glued the rear. During operation the backplane electrode is often set at half the positive potential of the anode electrodes, to form a repulsive field for ions and thus protect the front surface from ion accumulation.

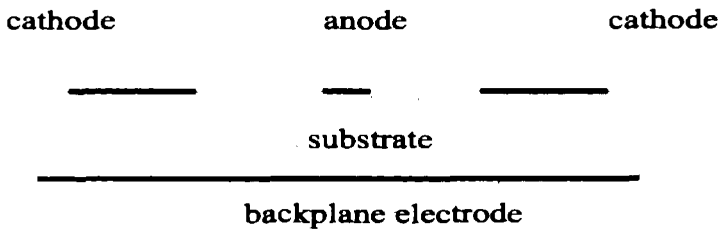

Figure 2.4 Microstrip with backplane electrode

However, the backplane electrode method is unable to solve the ion accumulation problem completely. The gain drop of MSGC detector with backplane can also be observed under high incident irradiation flux. To enhance the repulsive field, the potential of the backplane electrode can be increased to the same as that of the anode. But the intensive repulsive field can have a negative influence on the ion collection, and therefore the response time as well as spatial resolution of MSGC detector.

2.2.2.2 *Ion implantation*

Instability and gain modification of MSGCs, that could be attributed to the charging up of the insulating substrate between electrodes, can possibly be avoided by reducing the surface resistivity of the substrate by ion implantation. In ion implantation, dopants are introduced into a substrate directly in the form of ions, by bombardment of the substrate surface with an accelerated ion beam. These beams are generated by ion implanters which are really 5 ~ 200 keV high current linear particle accelerators with elaborately designed magnetic coils used for focusing and deflecting of ion beam. Since implant densities required implant as high as 10^{18} ions/cm^2, it turns out that this method tends to be expensive and imposes a constraint on the maximum size of the detector.

Ortuno-Prados et al tested MSGC prints fabricated on the quartz substrate with carbon implantation [15]. Experimental results showed that performance of the ion implanted substrate MSGC detector is unsatisfactory. The gain decreased by 57% in 24 hours and gain variation of ±24% was found over 1 cm^2 area. Recently, the group at CRPP reported on plastic (Kapton) prints modified by ion-implantation with good high rate performance, but they found it hard to control the ultimate surface resistivity produced during the implantation process [16].

2.2.2.3 *Electrical conductive substrate*

Resistivity of glass substrates can also be changed by doping sodium or iron oxide during manufacture. Those special doping glass substrates can be also used for MSGC prints to avoid ion accumulation on surface. However, the mechanical property of the glass will also be changed by the doping process. Usually, those doped glasses are brittle, which makes it difficult to fabricate MSGC prints of large area. Additionally, like ion-implantation, it is difficult to ensure the resistivity of glass in a certain region by controlling the doping process. Commercial iron-loaded glasses are also extremely expensive.

Furthermore, a gain drop of MSGC detector with sodium doped glass has been observed [17]. This gain drop occurred during the first few hours of operation of the chamber, which did not depend on radiation rate and had a global nature. This gain variation has been explained as a result of alkali ion motion. Since a high voltage is applied between anode and cathode in a MSGC, the alkali ions in glass substrate migrated from one electrode to another. Consequently, the conductivity of the glass substrate will be changed.

2.2.2.4 *Substrate coated with conductive layer*

A thin conductive layer on the top of substrate can also be employed to solve the ion accumulation problem in a MSGC detector. This conductive layer can be formed either by evaporation deposition or standard sputtering techniques. Since only a thin layer was used to remove surface charge, one advantage of a coated substrate over a conductive glass substrate is less leakage current. Ion migration is avoided as well.

Brons et al deposited semiconductor layers on the surface of glass substrates for MSGC prints [8]. The semiconductor layer was formed by evaporating copper or germanium on the top of substrate, followed by a heating process at 70°C in air. The sheet resistivity of the resulting film was in the order of 10^{12} Ω/square. The x-ray detector with those MSGC prints could be operated under radiation flux as high as over 10,000 photons/(s·mm^2) without gain drop. Salomon & Chapman [11] realized the passivation of MSGC detectors by sputtering nickel and nickel oxide layers on the surface of various substrates, such as glass, Tedlar and Upilex. Those MSGC detectors were also operated under high irradiation rate of 6,000 photon/(s·mm^2) without gain drop. Long term observation on MSGC detector operation has also been made. No performance variation has been found for a period of over 30 days. However, up until now the reproducibility of the nickel oxide films has been poor. Hence finding a technique to produce stable, reproducible films is the major aim of this thesis.

It should be mentioned that an alternative geometry, called a microgap chamber, was proposed to avoid the ion accumulation problem in radiation detection. We also proposed two methods to implement a microgap detector [see Appendix 2].

2.2.3 Nickel oxide passivation

In this thesis, the nickel oxide passivation was selected to decrease the surface resistance of substrates and solve the ion accumulation problem in a MSGC system. It has been reported [18] that both the ion implantation and nickel oxide passivation can be used to solve the ion accumulation in MSGC. However, it is not easy to control the sheet resistivity of the passivation film with the ion implantation [18].

There are strict requirements for the nickel oxide passivation layer on sheet resistivity (10^{12}~10^{14}Ω/square) and thickness (~ 50nm). The reason for the high resistivity requirement is that a high voltage is applied between anodes and cathodes during the operation. Meanwhile, the nickel oxide film also functions as the conductive film to remove the accumulated ions. It is known that the gas gain is highly dependent on the electric field between the anode the cathode, the high surface resistivity is also necessary to avoid the field being affected very much. Theoretical analysis shows that the gas gain can be as high as 40000 when the sheet resistivity is in the range of 10^{12} ~$10^{14}\Omega$/square [17].

Since the passivation layer covers all the detection area, including anodes and cathodes, the passivation layer should be thin enough that the electrons and the positive ions can penetrate the layer and be collected by the anodes and the cathodes.

Nickel oxide film deposition methods can be categorized as: evaporation, sputtering deposition and electrochemical and chemical techniques. In this thesis, the nickel oxide passivation was done by the DC sputtering deposition. As discussed above, control of the deposition process is very important because a high sheet resistivity is required for the passivation layer. For the sputtering deposition, the composition and structure of the film can be controlled by varying the deposition parameters (for example, oxygen flow rate). Another advantage of the sputtering deposition over the evaporation method is that the sputtering deposition can form a film with better coverage.

The reason of selecting sputtering deposition, rather than the chemical technique, is that the sputtering deposition is a non-contact, dry process. No caution has to be taken for the corrosion and contamination of the electrodes. Additionally, the microstrip structure on the substrate will also cause difficulty on the uniformity for some chemical method (for example, sol-gel deposition) when such a thin film is formed.

The difficulty of the passivation process is that the sheet resistivity of the nickel oxide layer is required in the range of $10^{12} \sim 10^{14}$ Ω/square. This desired sheet resistivity was achieved by controlling the nickel/oxygen ratio in the passivation layer. Therefore, the oxygen flow rate was carefully controlled when introducing oxygen to the gas chamber during the sputtering deposition. It is why in the sputtering deposition we used the nickel target rather than a nickel oxide target, with which a method should be found to strip the oxygen.

Another function of the nickel oxide passivation film is to alleviate the discharge between the anode and cathode. In MSGC, x-ray radiation is detected based on the avalanche amplification between the anode and cathode. However, the avalanche amplification may also be initiated by a single electron emitted from the cathode, which causes a discharge between the anode and the cathode. To avoid that, the microstrip structure can be covered with a layer of a material with a low secondary electron emission coefficient, like NiO. This is another reason that we select nickel oxide film as the passivation layer.

2.3 Print fabrication process

The MSGC prints were fabricated on glass substrates with some basic IC processes, which includes surface preparation, sputtering deposition, photolithographic patterning and passivation. Two kinds of glass substrates were used, one is a window glass of 3mm thickness from Northwest Lab, another is the quartz of 1mm thick from Schott. The size of those glass substrates is 7mm by 7 mm.

2.3.1 Surface preparation

Surface preparation is the first step in the fabrication process. The glass substrate surface is cleaned with RCA process [20] to remove contaminants, which allows those metallic microstrips to adhere firmly to the substrate.

2.3.2 Sputtering deposition.

For MSGC print fabrication, a layer of aluminum was deposited on the surface of a glass substrate. This metal layer will create the electrodes (both the anodes and the cathodes) of the MSGC print after being patterned. The thickness of aluminum film is around 1 μm.

The thickness of the MSGC electrodes also has an effect on the discharge between anode and cathode. By increasing the thickness of the microstrips, the field strength at the borders of the strips can be diminished. Compared with thin metal layer, a thick one is much more uniform. Another advantage of the thick electrode layer is to get a low resistance of the microstrips which is essential for a short rising time of the signal.

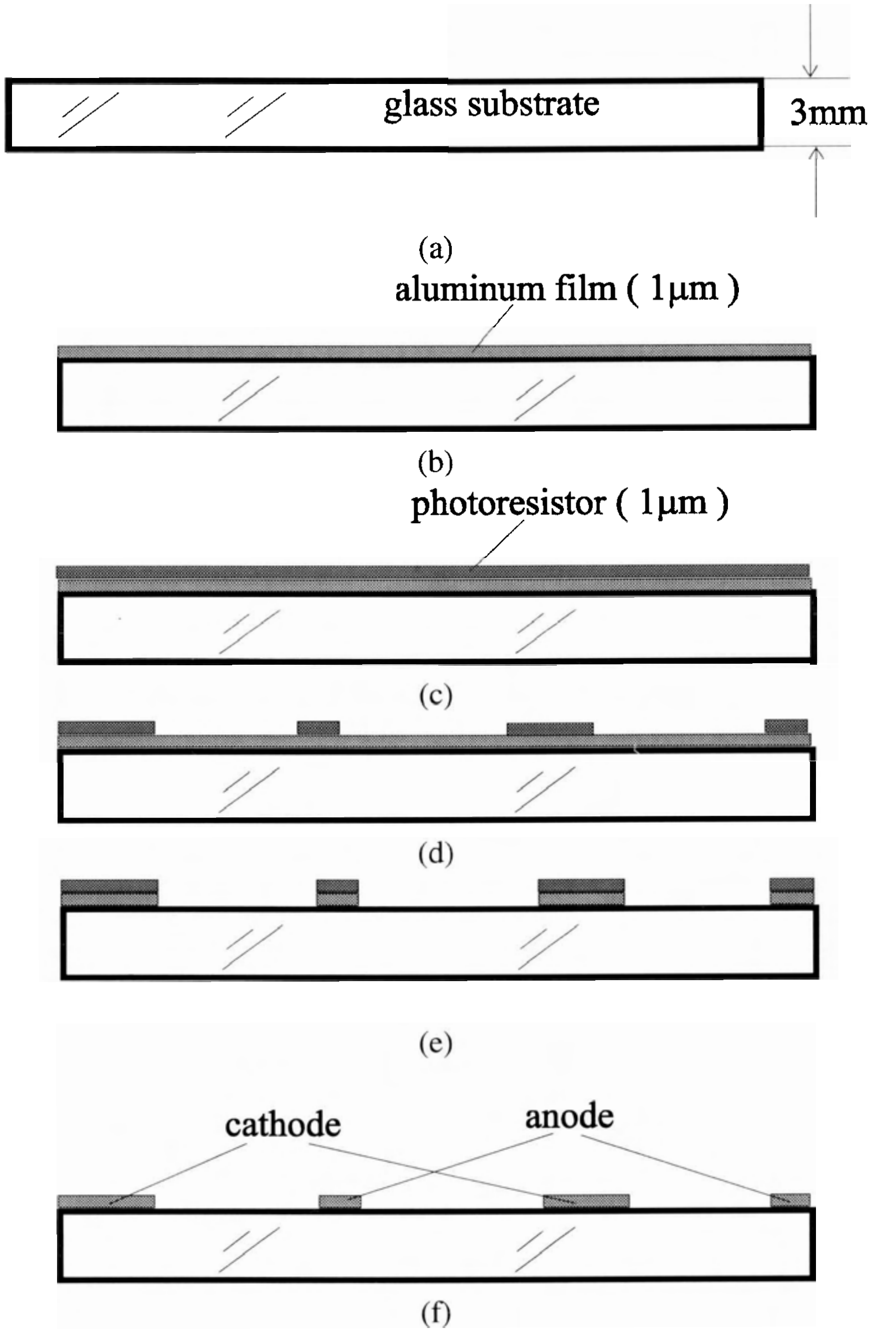

Figure 2.5 Photolithographic patterning process. (a) glass substrate after RCA cleaning, (b) aluminum deposition, (c) photoresist coating, (d) photolithographic patterning, (e) aluminum etching, (f) photoresist striping

2.3.3 Patterning

The patterning procedure is illustrated by Figure 2.5(c) through (f). First, a layer of positive photoresist (SPR2) was coated on the top of aluminum layer. Before photoresist application, the substrate with aluminum layer was cured in soft baking oven for 20 minutes at 100°C, to remove molecular water and improve the adhesion of the photoresist to the aluminum layer. When spin-coating of the photoresist, the spinner rotation speed of 4000 rpm was used for 30 seconds, which resulted in a layer of 1 µm thick photoresist on the top of the aluminum layer. Following resist application, the glass substrate was also cured in soft baking oven for 20 minutes at 100°C to remove remaining solvents in the photoresist layer. Next, the photoresist covered substrate was exposed to ultraviolet light through the MSGC mask. Considering reflection of the aluminum layer, the exposure time was 30 seconds. After being developed in AZ 351 developer, the structure on substrate is shown in Figure 2.5 (d). The patterned photoresist structure was cured at hard baking oven for 25 minutes at 110°C, to enhance resistivity of photoresist to the aluminum etchant. Then the aluminum layer with photoresist mask was etched by the aluminum etchant at 50°C for 2 minutes, as shown in Figure 2.5(e). Figure 2.5(f) shows the final structure after photoresist striping.

The dimension of MSGC prints, which were fabricated with the procedure described above, was measured under an optical microscope. To test the uniformity of the photolithographic process, we measured the width of the anode strips, cathode strips and anode-cathode gaps in the center and four corners of the MSGC print. The measurement results are listed in table 2.1 for a typical print. From table 2.1 it can be seen that the variation of the microstrip width is less than 5%. By comparing with the dimension of the mask used in fabrication, the over etching rate is also under 10%.

Table 2.1 Measurement results of MSGC print dimensions

	anode (μm) (±0.3μm)	cathode (μm) (±0.3μm)	anode-cathode gap (μm) (±0.3μm)
mask	21.1	91.0	146.8
center	19.8	89.1	148.5
corner 1	20.2	90.3	147.3
corner 2	20.4	89.8	147.4
corner 3	20.7	90.6	146.9
corner 4	20.6	89.9	147.3
average	20.34	89.94	147.48
σ	0.358	0.568	0.602

2.3.4 Passivation with nickel oxide film.

For passivation, the MSGC prints were covered with a thin nickel oxide film to overcome the charge accumulation on surface of glass substrate. The detailed fabrication process will be presented in chapter 4.

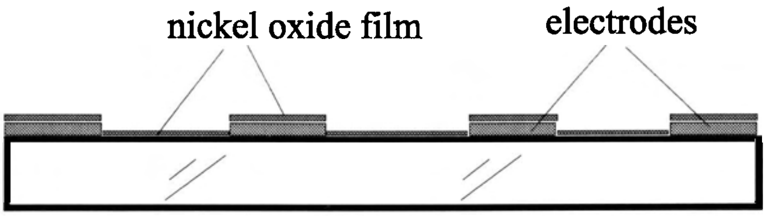

Figure 2.6 MSGC print passivated with nickel oxide layer

2.4 Summary

The design and fabrication of the MSGC print were discussed in this chapter. We also discuss the discharge phenomenon in MSGC, which limits the maximum gain of MSGC. Based on those considerations, a new mask of MSGC patterns was designed for imaging x-ray detector. Previous works on charge accumulation were reviewed, and the decision was made to use standard sputtering techniques for passivation of MSGC prints with nickel oxide film. The fabrication processes were also described.

Chapter 3 Microstrip Gas Chamber Detection System

A microstrip gas chamber detection system consists of the microstrip gas chamber, the gas supply system and the electronic read-out circuitry. The signal from anode strips appears as a charge pulse of tens nanosecond duration, whose amplitude corresponds to $10^3 \sim 10^4$ electrons. Therefore, the electronic read-out circuitry of microstrip gas chamber detection system has to meet the requirements of the high sensitivity and the high response speed in the same time.

In this chapter, a microstrip gas chamber detection system is described. The QPA02 [19], a high speed and low noise preamplifier designed in Fermi Lab, is tested and used as read-out circuitry in that detection system. Performance of detection system with MSGC prints is also studied.

3.1 Microstrip gas chamber

The gas chamber is the sensing element of a x-ray radiation detector based on gas ionization. As shown in Figure 3.1, the MSGC print was mounted on the printed circuit board (PCB). The aluminum frame with a thin aluminized nylon window covered the print and a drift electrode, and formed the gas chamber. A copper mesh of 0.5 mm spacing is mounted about 3mm above the print and serves as the drift electrode. When a negative high potential (around -2000V) is applied to the drift electrode, the drift field between the mesh plane and the print is built up to collect electrons created in the ionization produced by x-ray photons. A voltage is also applied between anodes and cathodes in the MSGC print for avalanche amplification.

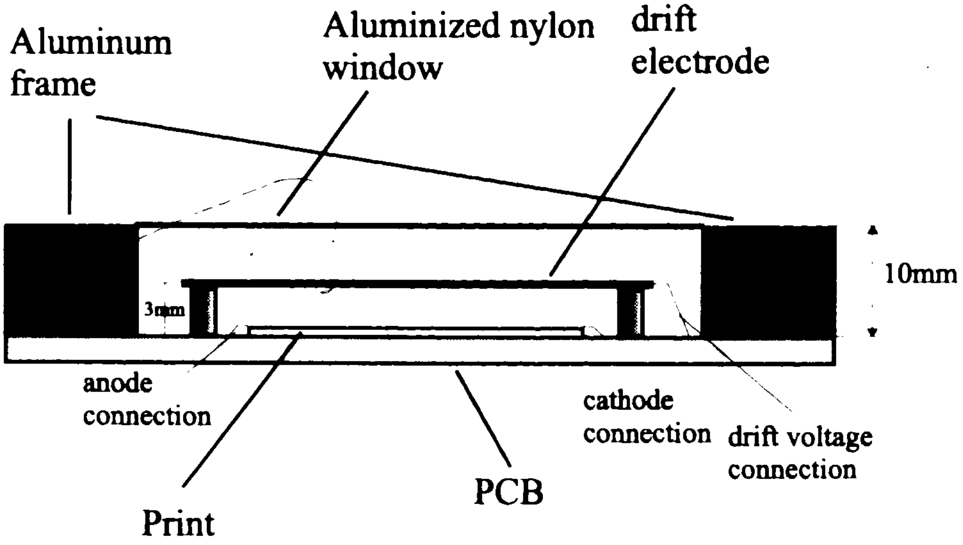

Figure 3.1 The cross section view of the microstrip gas chamber

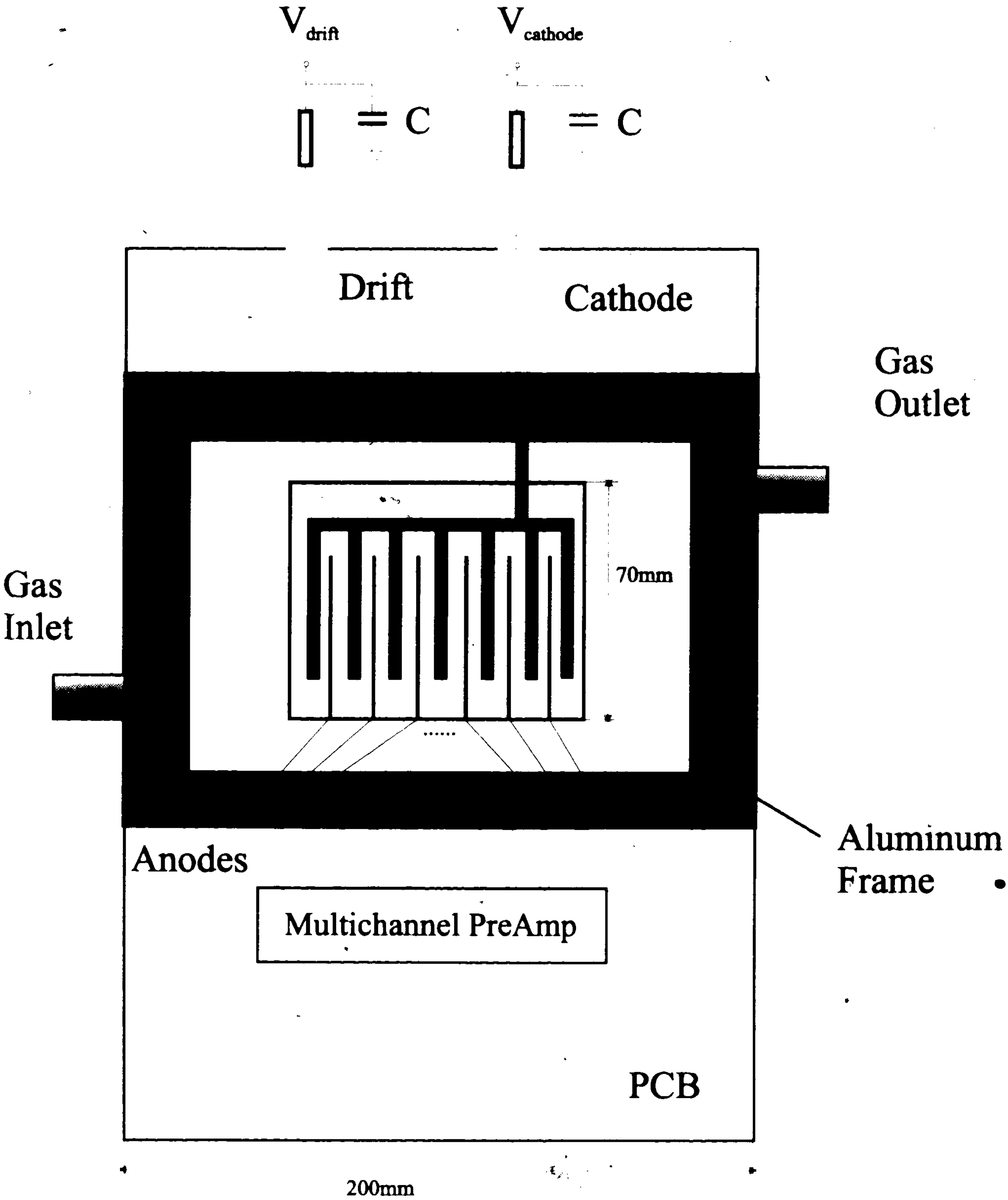

Figure 3.2 The top view of the microstrip gas chamber

Figure 3.2 shows the top view of the gas chamber. From Figure 3.2, it can been seen that the application of operating potentials and the extraction of signals is performed by metal strips on the surface of PCB. RC circuits were employed in both drift and cathode circuitry to filter out high frequency noise from high voltage DC power supplies. Resistors also work as protection resistance for anode-cathode and anode-drift discharges. Each anode is grounded through a 100 kΩ resistor (not shown in Figure 3.2). There are one gas inlet and one gas outlet to supply the ionization gas for the chamber. Figure 3.3 shows the electrical connection diagram.

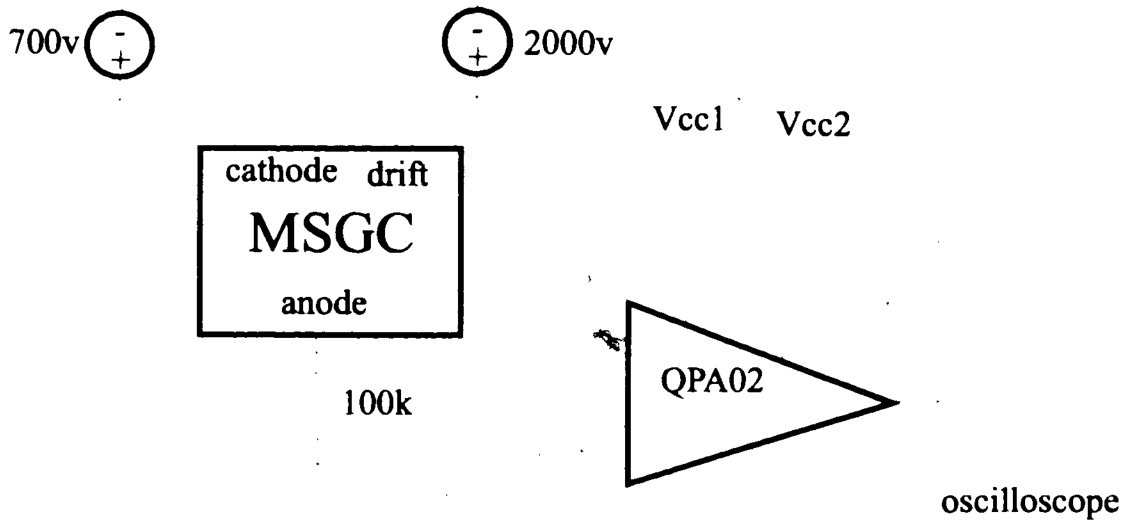

Figure 3.3 The diagram of the MSGC wiring

The experimental setup for preliminary measurements is shown in Figure 3.4. To eliminate influence of electromagnetic noise in air, the chamber under test was mounted in a grounded metal box. Power supplies, multiple channel preamplifier and the oscilloscope used in the measurement were carefully grounded as well with a common ground point. In the first testing, groups of anode strips were connected together to the readout electronics. In measurement, an ^{55}Fe radiation source of 100μCi was used as x-ray source (3.7×10^{6} photons/s), which was put on the top of the window.

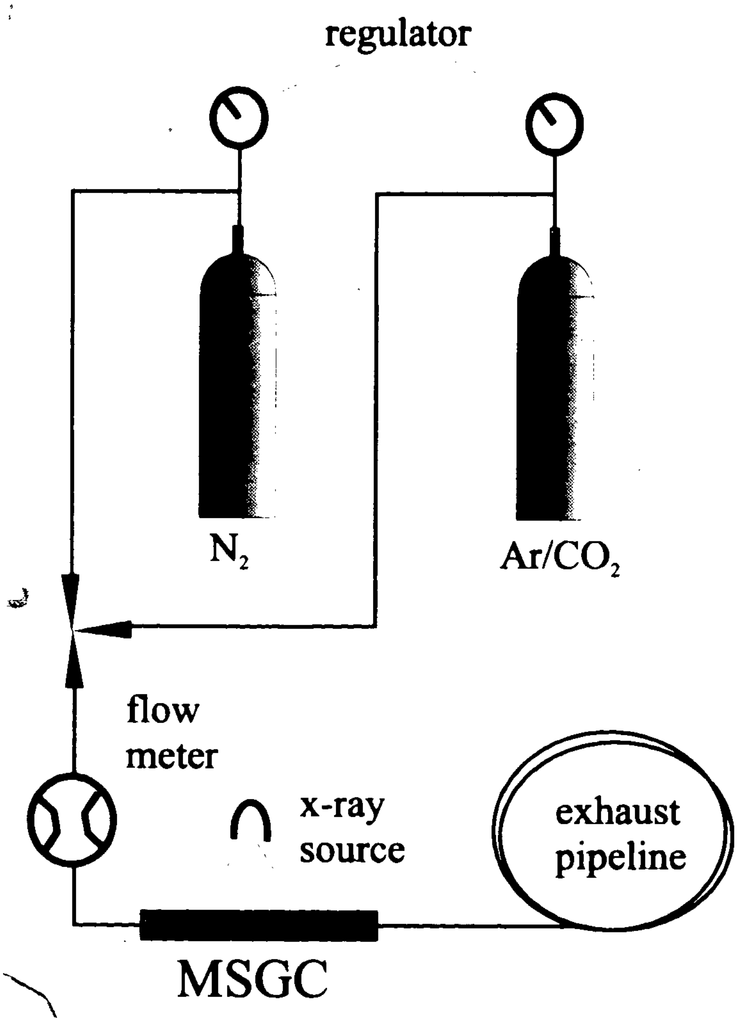

Figure 3.4 Experimental setup

The gas system included the nitrogen gas, the ionization gas and exhausting gas pipelines, all made out of quarter inch diameter copper tubing. Copper was used because the DME gas attacks plastic tubing. Both gas supply pipelines contained mass flow meters and regulators. The exhaust gas pipeline, which exhausted into a fume hood, was a copper tubing over 20 feet length, to prevent air flowing backward into gas chamber. The dry nitrogen gas pipeline was used to continuously flush the gas chamber when it was in idle status to prevent water vapour being adsorbed by the microstrip print. For operation of the MSGC, the gas supply was switched to the ionization gas pipeline. The ionization gas must be allowed to flow for at least 30 minutes prior to making the first measurement. Ionization gases used in the measurements were either a 85:15 mixture of argon and carbon dioxide (CO_2) or a 90:10 mixture of argon and dimethylether (DME). Both of them have been used successfully.

Another important parameter, which must be considered in gas chamber design, is the gas gap, i.e. the distance between drift electrode and print. The gas gap also plays a role in both gain and spatial resolution of microstrip gas chamber detector. From the requirement of the short charge collection time, we have learned that the gas gap has to be as narrow as possible (about 3mm). In addition, the spatial resolution is also related to divergence of incident x-ray and electron diffusion. By reducing the gas gap, the traveling path of x-rays and ionized electrons is shortened. Deterioration of the resolution due to divergence and diffusion is thus be alleviated.

The width of the gas gap also determines the absorption efficiency of x-ray radiation and the dimension of the avalanche region, which is critically related to the gain of the gas chamber. The avalanche amplification efficiency deteriorates when reducing the gas gap. But we know that the drift field strength is larger for smaller gas gap. Since the drift field induces positive charge over all conductors on the substrate, the higher drift field will lead to more positive charge on anodes. As a result, the gas gain, which is mainly ruled by the anodic charge, will rise. Additionally, the maximum gas gain is mainly controlled by the discharge of the cathode. In contrast, the increased drift field will reduce the charge density on the cathode, resulting in a higher breakdown voltage and thus a higher maximum gas gain.

3.2 QPA02 Amplifier

The output electrical signals from MSGC were amplified, measured and displayed with the readout electronic system. The readout electronic system consists of a QPA02 amplifier and the Tektronix 2025 digital storage oscilloscope. The QPA02 was a high speed bipolar transresistance charge amplifier. It converted an impulse of electric charge to a fast voltage pulse. It was originally designed as a silicon strip amplifier in Fermi Lab. The gain of QPA02 was claimed in the order of 15mV/fCoulomb while the rise time was less than 38 ns.

3.2.1 Schematic of QPA02 amplifier

The schematic of QPA02 amplifier and its pinout can be found in Appendix 1.

3.2.2 Performance of QPA02 amplifier

Before connected to the MSGC, the gain of the QPA02 amplifier was measured. For all tests, the input was a voltage signal generated from a SRS D5345 function generator and the output signal was measured with the Tektronix digital storage oscilloscope.

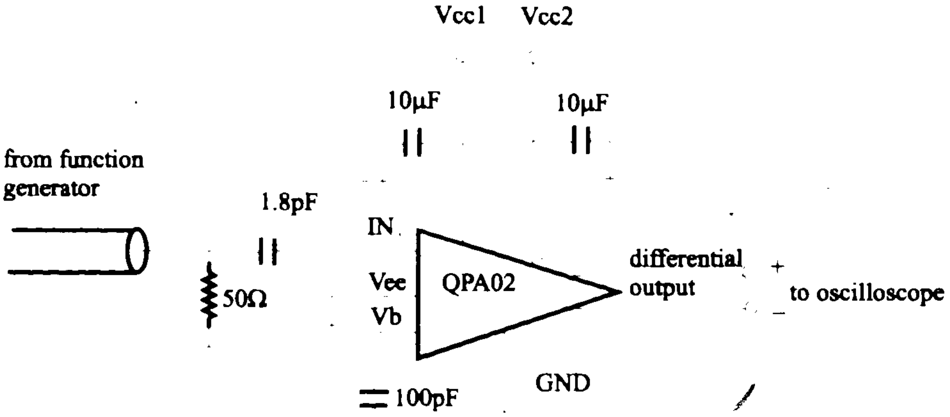

Figure 3.5 QPA02 test circuit diagram

Figure 3.5 is the diagram of the test circuit. Vee, GND and other common points are all referenced to the same low impedance ground plane. Bypassing capacitors (100pF) are used to filter out high frequency noise from DC power supplies, Vcc1 and Vcc2. To eliminate high frequency noise, Vb pad is also grounded through a bypassing capacitor.

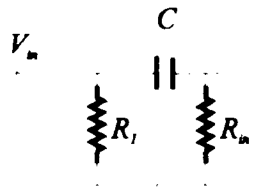

Figure 3.6 Equivalent input circuit

The square wave from the function generator was used as the testing input signal. Differentiated by a capacitor (1.8pF), the square wave voltage profile formed one positive and one negative pulses. Corresponding to those two pulses, the temporal profile of output signals from QPA02 was recorded, and the gain, response time and distortion of QPA02 amplifier were also investigated.

Suppose the input impedance of the QPA02 is R_{in} as shown in Figure 3.6. The duration of pulse differentiated by the capacitor C is represented as

$$\tau = \frac{1}{(R_l + R_{in}) \cdot C} \qquad (3.1)$$

If the amplitude of the input voltage signal is V_{in}, the corresponding charge on the capacitor is

$$Q = C \cdot V_{in} \qquad (3.2)$$

In our experiments, the capacitance of C was 1.8pF, the external resistor R_l was 50Ω and the input impedance of the QPA02 was approximately 200Ω. The charge of 1.8×10^{-15}C was generated when input voltage is 1V, for example.

Figure 3.7 shows the output response of the QPA02 for different input amplitudes. The output impulse was acquired with a digital oscilloscope which was operated in the

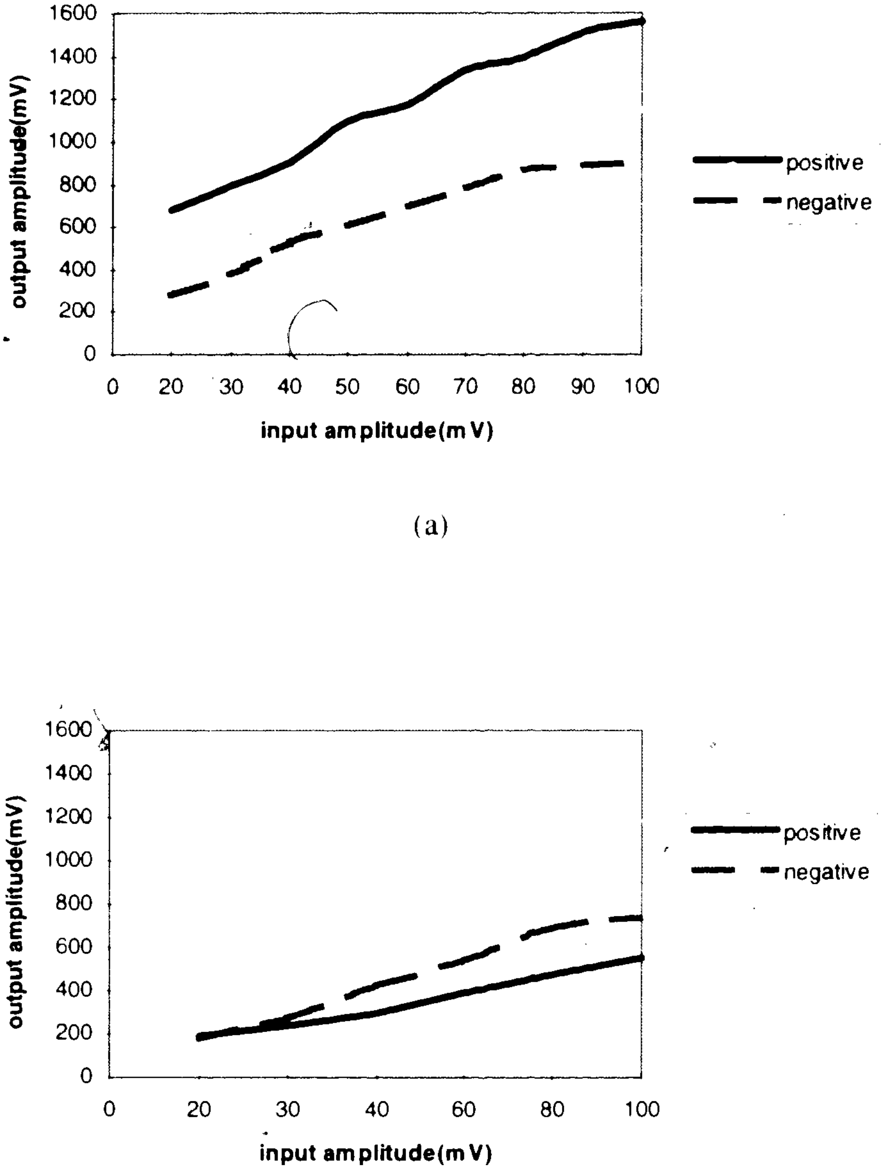

(a)

(b)

Figure 3.7 Curves of output amplitude vs. positive and negative input amplitude of QPA02 amplifier. (a) Vcc1 = 5.0V and Vcc2 = 4.1V, (b) Vcc1 = 5.5V and Vcc2 = 2.7V sampling mode with 50Ω input impedance to match the coaxial cable. From Figure 3.7(a) the gain for a positive input pulse was found to be much higher than that for negative input pulses when Vcc2 = 4.1V, which indicates that the QPA02 was not biased properly. With the equation (3.2), it was estimated that the gain for positive pulse was about 18.89mV/fC while the gain for negative pulse was about 7.79mV/fC. The saturation of the QPA02 happened to the negative pulse when input amplitude is around 80mV, corresponding to the charge of 144fC.

Figure 3.7(b) lists the output vs. input curve when the QPA02 was biased with Vcc1 = 5.5V and Vcc2 = 2.7V. Under this circumstance, the output response for positive input pulse was almost the same as for the negative input pulse. However, the gain dropped to 5.28mV/fC. The QPA02 amplifier went into oscillation status when Vcc1 was 5.0V and Vcc2 was from 2.9V to 4.0V.

Figure 3.8 is the plots of the measured impulse response for the charge input of 36 fC when the QPA02 was biased by Vcc1 = 5.5 V and Vcc2 = 2.7 V. The charge was calculated from input pulse amplitude based on the Equation (3.2).

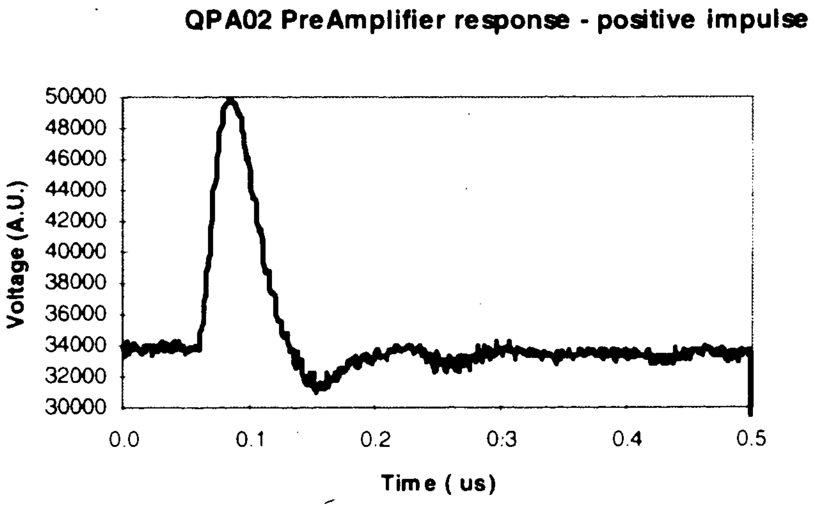

(a)

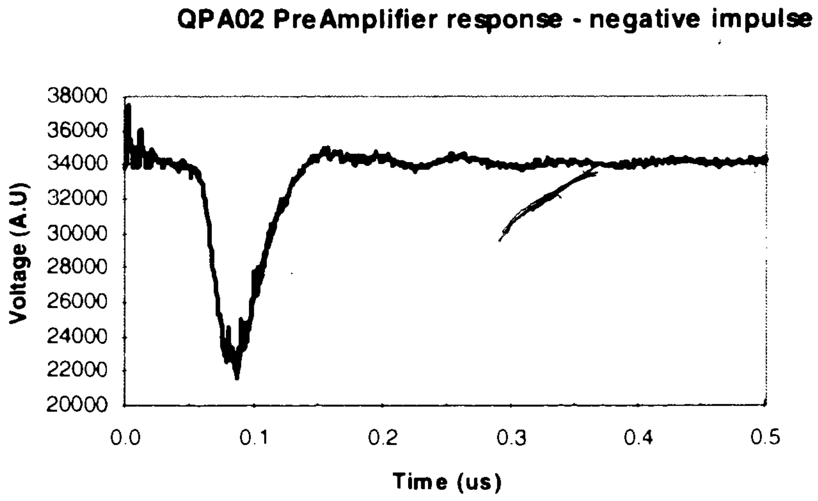

(b)

Figure 3.8 Impulse response of QPA02 (a) for positive input, (b) for negative input

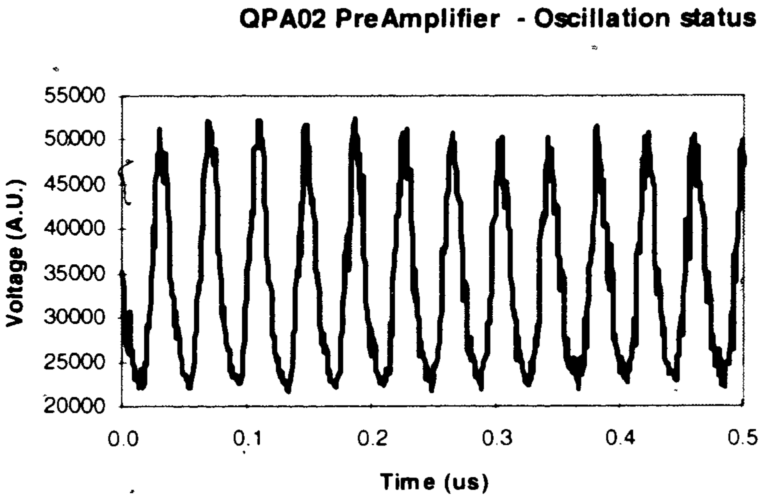

Figure 3.9 Oscillation status

Figure 3.8(a) and (b) shows the impulse response plots of the QPA02 amplifier for the positive input and the negative input, respectively. The rising time was about 40ns and the time of falling to base line was about 60ns. Those two curves show that the QPA02 has identical rising and falling times for the positive input and the negative input.

The oscillation behavior of the QPA02 amplifier is also shown in Figure 3.9. With Vcc1 = 5V, the QPA02 was oscillating when Vcc2 was in the range from 3.0V to 4.0V.. The oscillating frequency was around 25 MHz, and it kept constant when Vcc2 was adjusted from 3.0V to 4.0V. The amplitude of oscillation had a maximum value when Vcc2 was 3.6V. Both the source impedance at the input end and the load impedance at the output end could change the oscillation frequency and critical DC voltages (Vcc1 and Vcc2) of QPA02 amplifier. For example, the oscillation frequency became 10 MHz when the oscilloscope at output end was operated at 1MΩ mode.

3.2.3 Performance of QPA02 amplifier connecting with the MSGC

The QPA02 amplifier was originally designed for silicon strip detectors. Due to its large gain and wide bandwidth, the QPA02 amplifier can be in oscillation mode, which is dependent on external conditions, such as the biasing condition, the input and output impedance. The MSGC represents a clear example of multi-electrode distributed transmission line. The exact response of the detectors depends therefore on such parameters as the resistance of strips, inter strip capacitance and so on. Before the measurements of x-ray radiation was carried out, the performance of the QPA02 amplifier connected to gas chamber was measured.

When connected to gas chamber the QPA02 amplifier was biased in the same way as shown in Figure 3.5, except the coupling capacitor and 50 Ω resistor were removed. Two anodes of the MSGC print are grouped together, and capacitance between anodes and cathodes is 15 pF. Under those conditions, the QPA02 was in stable amplification region only when Vcc1 was less than 2.7 volts.

The response of the QPA02 amplifier was measured by applying a square wave signal to the cathodes. Figure 3.10 shows the output amplitude vs. input amplitude curve. It can be calculated that the gain of the QPA02 amplifier was about 7.8mV/fC. It is known there are around 40,000 electrons generated by avalanche amplification of MSGC for each ^{55}Fe event. Correspondingly, the output pulse height of QPA02 amplifier was expected to be of the order of 50 mV. Hence, the signal from the MSGC was predicted to be detectable with the QPA02 amplifier.

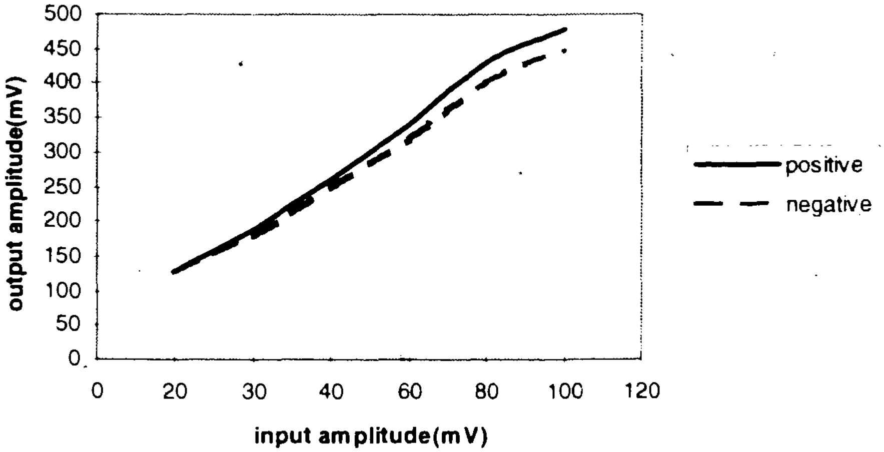

Figure 3.10 Output vs. input curve of QPA02 connected to MSGC

3.3 Observation of X-ray radiation signals

Before the coating experiments, the performance of the detection system was also tested with 5.9keV x-ray photons from the ^{55}Fe X-ray source. As shown in Figure 3.11, the output signal of QPA02 amplifier was sampled by Tektronix 2232 digital storage oscilloscope. The data, digitized by Tektronix 2232, were collected by a PC through the RS232 port and stored in the hard disk.

During detection, the oscilloscope could be operated either in analog mode or digital mode. A 50Ω terminator was used to decrease the load impedance of QPA02 amplifier and increase the signal response time. Since random voltage pulses were being observed, it was essential to set trigger level for the oscilloscope, to capture and display those random signals. It was found that for analog mode, the optimal time sweep of oscilloscope was 0.5μs/div, whereas for digital mode the sampling interval was 50ns.

Figure 3.12 is the photograph of the typical signal profile for ^{55}Fe source. The rising time of pulse was about 50 ns and falling time is about 100ns, and the amplitude is 120 mV.

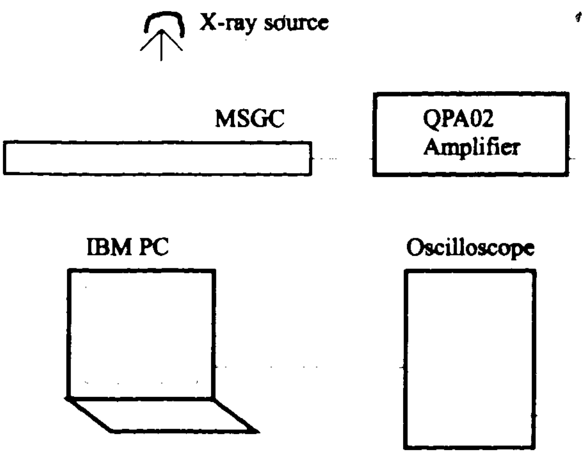

Figure 3.11 Schematic of data collection system for x-ray detection

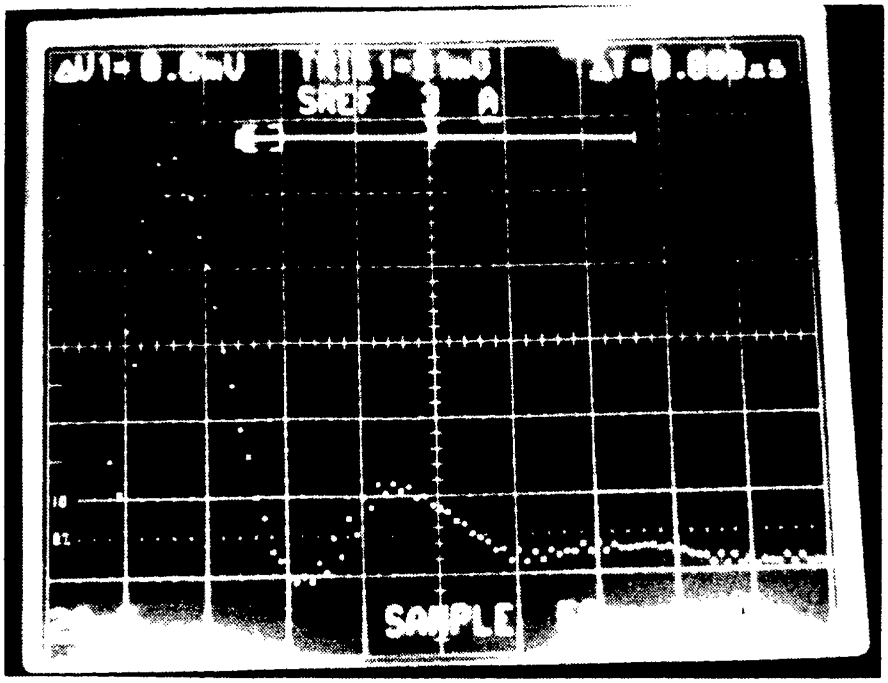

Figure 3.12 The typical pulse profile of x-ray signals

3.4 Summary

The readout electronics are described in this chapter. The performance of QPA02 preamplifier, which is used as the preamplifier of the MSGC detector, is studied. The optimal biasing conditions of the QPA02 amplifier when connecting with the MSGC chamber were obtained. The gain of the QPA02 preamplifier was as high as 7.8mV/fC. With the QPA02 amplifier, a x-ray detection system was built up, including data display and data collection by a computer. Preliminary experimental results showed that output signal amplitudes corresponding to x-ray radiation were as high as 100 mV. Therefore this x-ray detection system could be used in the study of MSGC performance and MSGC print testing.

Chapter 4 Passivation of MSGC Prints with Nickel Oxide Film

As discussed in chapter 1 and chapter 2, the MSGC has been confronted with the problem of short term gain instabilities during its operation, particularly if exposed to high particle fluxes. The gain variation of the MSGC is due to the accumulation of ions generated in the avalanche on the surface of the insulating substrate. It has been shown that the effect can be avoided using a substrate with decreased surface resistivity (10^{11} - 10^{14} Ω/square) [14].

The glass substrate, however, has a very high surface resistivity (over 10^{18} Ω/square). A surface treatment should be applied to the glass substrate to achieve the desired surface resistivity. In this thesis, the reproducibility of eliminating the charging problem by passivating the glass MSGC prints on the top of electrodes before assembling the MSGC has been investigated. The desired surface resistivity was achieved by sputtering a thin layer of nickel oxide on the top of the electrodes of the MSGC print. In the nickel oxide deposition process, plasma was generated with argon gas and a thin nickel (~50nm) layer was deposited in oxygen ambient. The process was controlled by a computerized system.

In this chapter, the sputtering process is introduced briefly. The deposition process of nickel layer and post processing are described. The electrical behavior of the nickel oxide film is observed. A comparison between nickel oxide films made in the different oxygen ambient is also made. Auger spectrometry was employed to analyze the composition of the nickel oxide film and the influence of the post baking process.

4.1 Passivation process

4.1.1 Nickel Oxide Deposition

The passivation of a MSGC print was accomplished by sputtering a thin nickel oxide layer on the top of microstrips in School of Engineering at Simon Fraser University. After the MSGC prints were loaded onto sputtering machine chamber, the chamber was pumped down to 1×10^{-6} torr by a two stage diffusion vacuum system. The argon and oxygen gases were then introduced to the vacuum chamber. The preset vacuum pressure was maintained by controlling the gas flow rates with a computer controller. For example, when chamber pressure was set to 3 mtorr, the flow rates were controlled at 1.9 sccm/min for argon and at 0.6 sccm/min for oxygen, respectively. The system was ready for sputtering deposition when the gas flow rates were stable. The passivation process consisted of three steps: sputter target cleaning, nickel deposition and post heating.

(1) Target cleaning. Before depositing nickel on MSGC prints, a sputtering preclean is done with the prints protected by the shuttle. The nickel target was sputtered on the shutter for over 100 Watt × min. The purpose of this process was to remove impurities on the surface of the nickel target. Furthermore, since the sputtering process was conducted in argon/oxygen ambient, it was expected that a fresh nickel oxide layer would be formed on the top of nickel target after the cleaning process.

(2) Deposition process. The nickel layer was deposited by a DC sputtering process. The typical specifications of sputtering process were as following:

base pressure: 1.2×10^{-6} torr
Ar flow rate: 3.0 sccm/min
O_2 flow rate: 3.0 sccm/min
DC voltage: 442 V ~ 330 V
DC current: 0.055 A
Energy: 100 Watt×minutes

In the deposition process, the sputtering machine was operated in the current controlled mode. The DC current was set to 0.055 A, and DC voltage between target and MSGC prints was measured as 442 V. The total energy for nickel layer deposition was around 100 Watt × minutes, which resulted in the thickness of nickel film being approximately 50 nm. To protect the bonding pads from the nickel deposition, those pads were covered with scotch tape before loading the MSGC prints into gas chamber.

(3) Post baking process. After deposition, the resistivity of the nickel layer was relatively low, which was in the order of $10^6 \sim 10^9$ Ω/square. A post baking treatment was applied to the nickel film to increase its resistivity to the desired value. This baking process helped the nickel film convert to nickel oxide with a higher resistivity. This is discussed in more detailed in section 4.2.3.

The MSGC prints were heated by hot plate as shown in Figure 4.1. To monitor the temperature, a K-type thermocouple was made with Chromel and Alumel. During baking process, the thermocouple contacted the surface of the MSGC print. The temperature was read out with Digi-Sense thermometer. The temperature of baking process was controlled manually. The prints were heated at several temperature and maintained for 20 minutes under each temperature. After being baked at about 470°C for 20 minutes in open air, the resistance of the MSGC print was increased to the desired range.

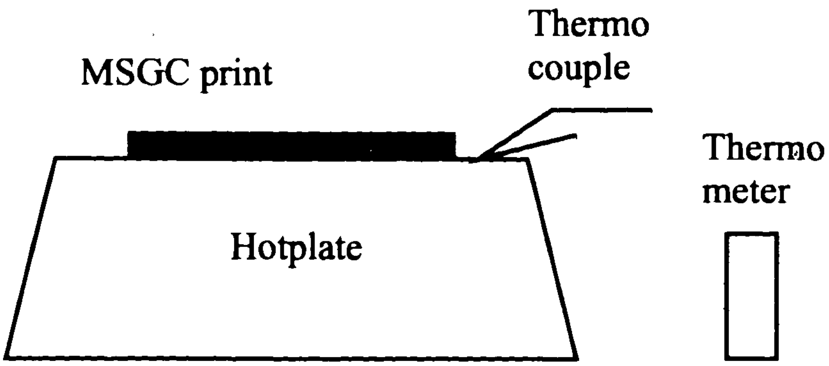

Figure 4.1 Post baking setup

4.1.2 Surface resistivity measurement

To determine the resistivity of the nickel/nickel oxide layer on the MSGC print, the resistance between one pair of anode and cathode pads was measured with a semiconductor parameter analyzer. Before presenting measurement results and calculating resistivity, the dimensions of the inter-digital structure of MSGC print are described. Figure 4.2 shows a pair of anode and cathode pads.

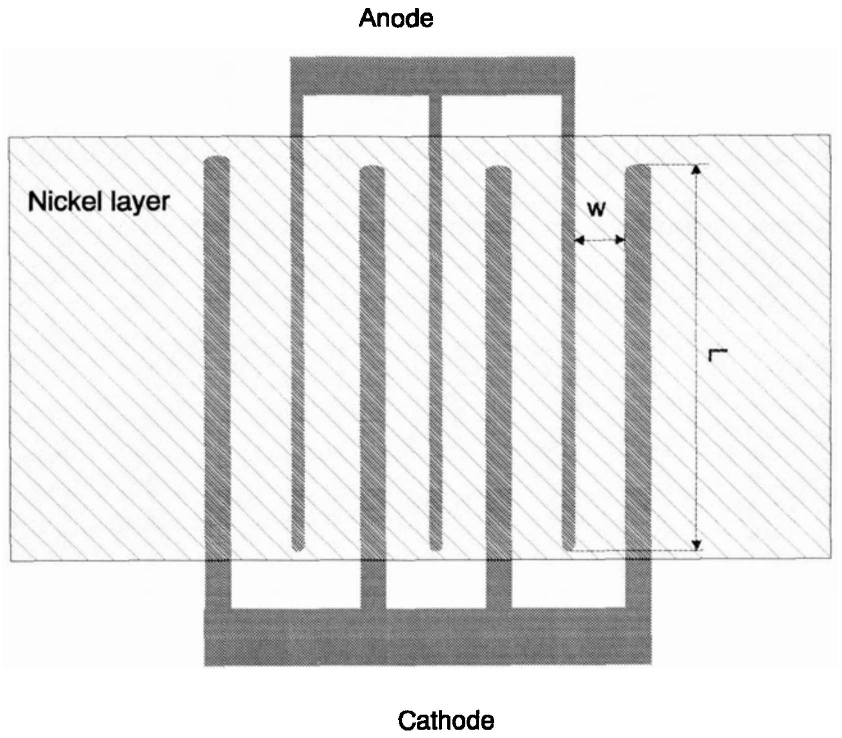

Figure 4.2 Layout of anodes and cathodes in the microstrip print

L is the length of the overlap between the anode and the cathode while W is the gap width between the anode and the cathode. Suppose a voltage V_0 is applied between the anode and the cathode, and the current through them is I. Then the sheet resistance is

$$R_s = 6 \times \frac{L}{W} \cdot \frac{V_0}{I} \qquad (4.1)$$

where the coefficient 6 is due to the six edges of those three anodes connected together. For our prints, $L \cong 5$ cm and $W \cong 150$ µm.

The resistance of the cured nickel film was measured with the semiconductor parameter analyzer in open air. Since it required the measurement of a weak current (in the order of nA or less), the print was put on a shielding metal box to avoid external electromagnetic noise. The semiconductor parameter analyzer was also grounded and co-axis cables were used for all electric connections. During measurements the semiconductor parameter analyzer was operated at the diode I-V mode, in which a DC voltage was applied between the anode and the cathode, and the current through them was measured. The DC voltage was swept from 0 to 20 volts. The I-V characteristics of the nickel oxide film were recorded.

4.1.3 Experimental results

The nickel oxide films have been deposited under two different gas conditions. All the nickel oxide films have been applied with the post baking process for 20 minutes at 470°C. In this section the experimental results of the influence of oxygen density and the post baking process on the sheet resistance of the nickel film are presented.

4.1.3.1 Nickel oxide deposition in the low oxygen ambient

The first batch of samples were made when the flow rates for argon and oxygen gases were 3.0 sccm/min and 0.6 sccm/min, respectively. The ration between argon and oxygen density was 5:1. The I-V characteristic curves of those nickel oxide are shown in Figure 4.3.

It can be seen from Figure 4.3 that, the sheet resistivity of the nickel oxide film can be in the range of $10^{12} \sim 10^{14}\Omega$/square after post baking. However, for unknown reasons the nickel oxide films have nonlinear exponential like behavior of resistivity, as shown in their I-V curves of Figure 4.3. Thus, it was expected that the resistivity of the nickel oxide film would decrease dramatically as the applied voltage increased. Those prints coated with such nickel oxide film were assembled into the gas chamber. The leakage current was as high as 0.01 mA when the voltage between the anode and the cathode was 600V. It was equivalent to the sheet resistance of $1.5\times10^{9}\Omega$/square. Obviously, this leakage current is too large for x-ray detection, under which the signal could not be observable. Table 4.1 lists the sheet resistance of three nickel oxide films with different thickness. It shows that the sheet resistance increased about 5 times when the applied voltage increased from 10V to 20V.

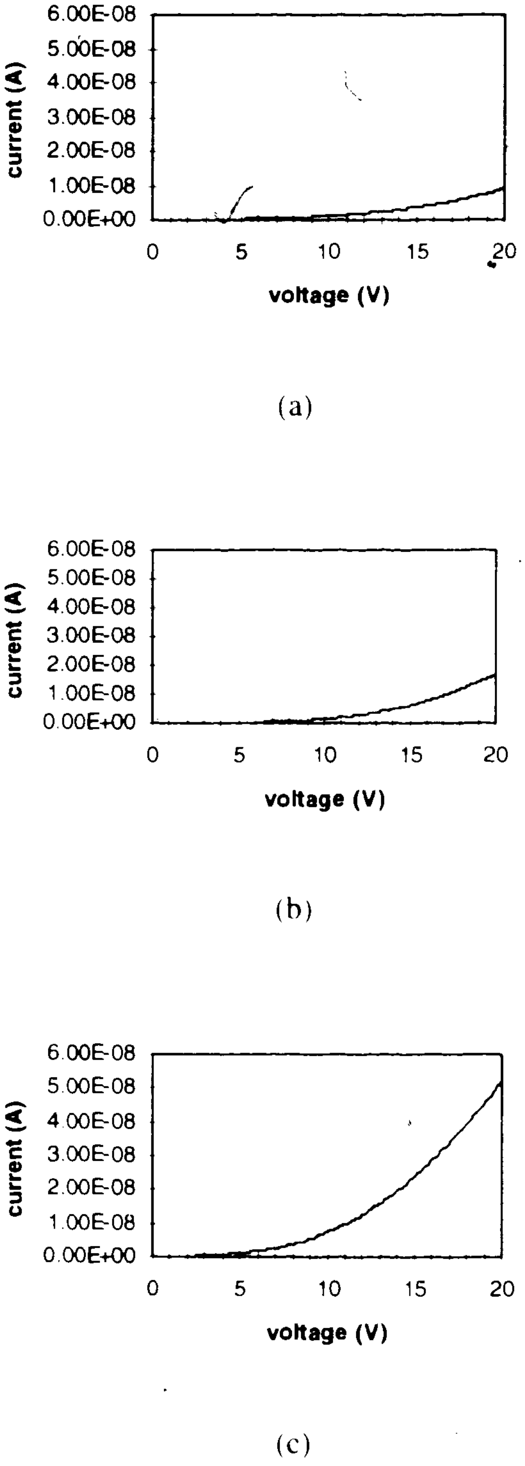

Figure 4.3 I-V curves of nickel oxide film of different thickness (a) 5 nm, (b) 25 nm, and (c) 50 nm when argon and oxygen flow rate ratio was 5:1

Table 4.1 Sheet resistance of nickel oxide films formed in the low oxygen gas ambient

Voltage (V)	Sheet Resistance		
	Sample 1 (5nm) Ω/square	Sample 2 (25nm) Ω/square	Sample 3 (50nm) Ω/square
10.0	1.27×10^{13}	1.08×10^{13}	2.06×10^{12}
11.0	1.09×10^{13}	8.42×10^{12}	1.71×10^{12}
12.0	9.41×10^{12}	6.69×10^{12}	1.44×10^{12}
13.0	8.16×10^{12}	5.40×10^{12}	1.23×10^{12}
14.0	7.10×10^{12}	4.44×10^{12}	1.07×10^{12}
15.0	6.21×10^{12}	3.70×10^{12}	9.41×10^{11}
16.0	5.45×10^{12}	3.13×10^{12}	8.39×10^{11}
17.0	4.81×10^{12}	2.68×10^{12}	7.54×10^{11}
18.0	4.25×10^{12}	2.32×10^{12}	6.85×10^{11}
19.0	3.78×10^{12}	2.04×10^{12}	6.26×10^{11}
20.0	3.35×10^{12}	1.80×10^{12}	5.78×10^{11}

Table 4.2 Sheet resistance of nickel oxide films formed in the high oxygen gas ambient

Voltage (V)	Sheet Resistance		
	Sample 1 (5nm) Ω/square	Sample 2 (25nm) Ω/square	Sample 3 (50nm) Ω/square
10.0	5.00×10^{13}	1.60×10^{14}	5.47×10^{13}
11.0	5.34×10^{13}	7.05×10^{13}	5.83×10^{13}
12.0	5.56×10^{13}	7.41×10^{13}	6.06×10^{13}
13.0	5.89×10^{13}	7.59×10^{13}	6.41×10^{13}
14.0	6.10×10^{13}	6.07×10^{13}	6.52×10^{13}
15.0	5.95×10^{13}	5.98×10^{13}	6.28×10^{13}
16.0	6.47×10^{13}	6.92×10^{13}	6.94×10^{13}
17.0	6.64×10^{13}	7.02×10^{13}	7.02×10^{13}
18.0	6.77×10^{13}	6.21×10^{13}	7.18×10^{13}
19.0	6.95×10^{13}	7.16×10^{13}	7.31×10^{13}
20.0	7.08×10^{13}	7.46×10^{13}	7.52×10^{13}

4.1.3.2 Nickel oxide deposition in the high oxygen ambient

The second batch of nickel oxide films was made by increasing oxygen flow rate to 3.0 sccm / min, which was 5 times larger compared with that in the first deposition. The density of oxygen was almost the same as the argon density in the sputtering machine

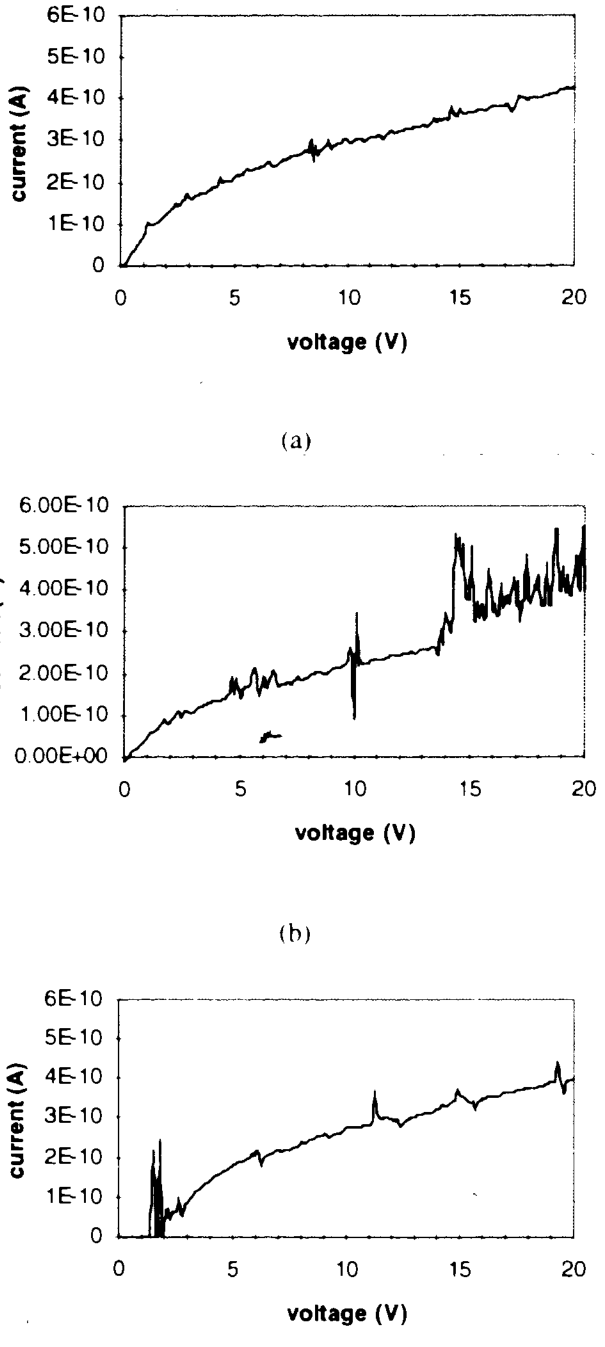

Figure 4.4 I-V curves of MSGC prints with different nickel film thickness. (a) around 50 nm, (b) around 25 nm, (c) around 5 nm when argon and oxygen ratio is 1:1

chamber. The resistivity of those nickel oxide films was in the desired range. Figure 4.4 shows the I-V curves of these nickel oxide films of different thickness after post baking process. The electrical characteristic of these nickel oxide films shows the sheet resistance of these three nickel oxide films of different thickness appeared linear when the applied voltage was over 5V. Table 4.2 lists the sheet resistance of nickel oxide films under the different applied voltage. The sheet resistance almost kept constant for every nickel oxide film. These MSGC prints were also assembled into the gas chamber for high voltage testing. No leakage current was detected when those prints were supplied high voltage (600V) in gas chamber, which meant that the total leakage current was less than 0.001mA.

4.1.3.3 Post baking process

The stability and the uniformity of the high oxygen nickel oxygen films was tested. A MSGC print passivated with the nickel oxide film deposited in high oxygen ambient was used as the testing sample. Table 4.3 through Table 4.7 lists the current values through anode-cathode pads when 20 V DC voltage was applied.

In the tables, A ~ F stand for different anode-cathode pairs in one MSGC print. Surface resistivity, which was calculated with equation (4.1), is also listed in those tables. As discussed above, the desired surface resistivity of substrate is in the range of 10^{11} - 10^{14} Ω/square. The measurement results show that the resistivity of nickel layer was in the desired range. From the variation of sheet resistance of different anode-cathode pairs it can also be seen that, the uniformity of nickel film was acceptable. After open to air 3 days the resistivity of the nickel film becomes stable.

To investigate the impact of the post baking process on the resistivity of the nickel oxide film, three MSGC prints were passivated with the nickel oxide films of different thickness. The same post baking processes were applied to those three MSGC prints. The deposition energy for those three films were 50 W×min, 25 W×min and 10 W×min. So, thickness ratio for those three films was roughly 5: 2.5 : 1. These prints were baked by the hot plate at various temperature. They remained at each temperature for 20 minutes. The resistance between the anode-cathode pair was recorded after each baking. Table 4.8 lists the resistance between the anode-cathode pair after each post heating process for the three prints.

Table 4.3 Measurement of resistance after baking, average resistance is 9.9×10^{10} Ω/square

anode	current (nA) at 20V	sheet resistance (Ω/square)
A	319	9.4×10^{10}
B	309	9.7×10^{10}
C	289	1.0×10^{11}
D	317	9.5×10^{10}
E	336	8.9×10^{10}
F	258	1.2×10^{11}

Table 4.4 Measurement of resistance 3 days after baking, average resistance is 1.16 $\times 10^{12}$Ω/square

anode	current (nA) at 20V	sheet resistance (Ω/square)
A	20.6	1.5×10^{12}
B	35.5	8.5×10^{11}
C	49.0	6.1×10^{11}
D	17.85	1.7×10^{12}
E	24.57	1.2×10^{12}
F	27.0	1.1×10^{12}

Table 4.5 Measurement of resistance 4 days after baking, average resistance is 6.9 ×10^{11}Ω/square

anode	current (nA) at 20V	sheet resistance (Ω/square)
A	93.0	3.2 ×10^{11}
B	42.0	7.1 ×10^{11}
C	19.0	1.6 ×10^{12}
D	51.9	5.8 ×10^{11}
E	81.1	3.7 ×10^{11}
F	52.0	5.8 ×10^{11}

Table 4.6 Measurement of resistance 5 days after baking, average resistance is 6.7 ×10^{12}Ω/square

anode	current (nA) at 20V	sheet resistance (Ω/square)
A	9.1	3.3 ×10^{12}
B	5.1	5.8 ×10^{12}
C	2.0	1.5 ×10^{13}
D	5.8	5.2 ×10^{12}
E	8.8	3.4 ×10^{12}
F	8.9	3.4 ×10^{12}

Table 4.7 Measurement of resistance 6 days after baking, average resistance is 5.2 ×10^{12}Ω/square

anode	current (nA) at 20V	sheet resistance (Ω/square)
A	16.7	1.8 ×10^{12}
B	9.3	3.2 ×10^{12}
C	2.0	1.5 ×10^{13}
D	5.1	5.9 ×10^{12}
E	10.3	2.9 ×10^{12}
F	12.0	2.5 ×10^{12}

Table 4.8 Resistivity of nickel films after various post heating processes

Print	Deposition power	Initial resist.	resist. (100°C)	resist. (150°C)	resist. (200°C)	resist. (240°C)	resist. (300°C)
A	50 J	20.3 Ω	22.1 Ω	22.9 Ω	27.1 Ω	41.7 Ω	16 MΩ
B	25 J	19.8 Ω	21.4 Ω	25.1 Ω	63 Ω	2.3 kΩ	11 MΩ
C	10 J	38.8 Ω	51.7 Ω	151 Ω	5.79kΩ	1.37MΩ	10 MΩ

When the prints were heated to 470°C, the sheet resistivity of all the prints is almost the same and in the order of 10^{14} Ω/square.

From the experimental results it can be observed that the surface resistivity of the MSGC print was not inversely proportional to the thickness of passivation layer. The fact can be explained as following: The nickel on the surface of the print was oxidized during the post heating process and formed nickel oxide, which was a good insulating layer. However, the surface molecules of the nickel oxide layer played a very important role on conductivity so that the final resistivity of nickel layer was independent of the thickness of the nickel oxide layer. It can also seen from Table 4.8 that the print A (around 25 nm thick) starts to increase in resistance at 300°C whereas the print C (around 5 nm thick) starts to increase in resistance at 200°C. But all of them can reach the desired resistivity after being baked at 470°C. It should also be mentioned that the advantage of thicker passivation layer is its better surface coverage.

4.2 Testing of passivation film in gas chamber

With the QPA02 electronic readout, the performance of the passivated MSGC were tested. The preliminary trials were oriented to proving that the MSGC could sense X-ray radiation. For that purpose the MSGC print whose 20 anodes were grouped to a single readout channel was used. The MSGC was operated with either an 85:15 Ar/CO_2 or 90:10 Ar/DME gases, and was irradiated with a Fe^{55} x-ray source (100μCi). The characteristics of the signal from the MSGC, such as the temporal profile, the relation of peak height vs. cathode voltage and drift voltage were studied.

4.2.1 Temporal behavior of signal from MSGC

To study the effect of the drift field on the charge collection of the MSGC, the shape of the avalanche amplification signal at different supply voltages Vd was recorded. Figure 4.5 shows the typical pulse of the QPA02 amplifier for a Fe^{55} radioactive source. The MSGC was operated while cathode voltage was -700V and drift voltage was -2000V, corresponding to drift field of about 6700V/cm. The anode signal has a rise time of ~50ns and a fall time of ~50ns.

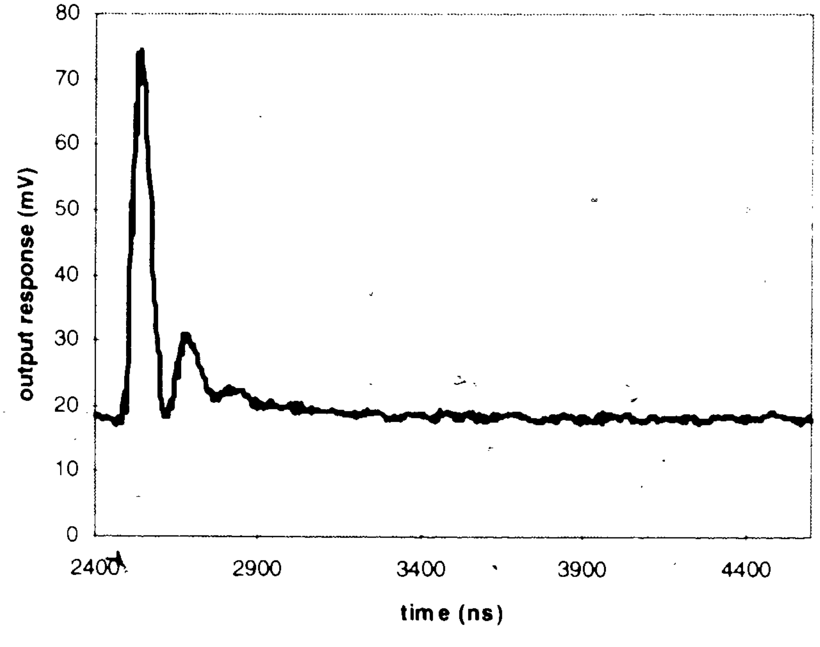

Figure 4.5 Output response of MSGC operated with Ar/CO_2 gas when V_c = -700V and V_d = -2000V

When the drift potential was dropped by a factor of two, i.e. -1000V, corresponding to drift field of about 3300V/cm, the peak height decreased but the pulse shape was essentially unchanged. That observation indicated that the drift field contributes to the gain of the MSGC but not to the response speed. As discussed in Chapter 2, the function of charge collection is performed by cathodes in the MSGC rather than the drift electrode as in the MWPC. Figure 4.6 shows the anode pulse recorded for the Fe^{55} radioactive source when the cathode potential was dropped to -630V. From Figure 4.6 it can be seen that the falling time is increased about 10% at that time.

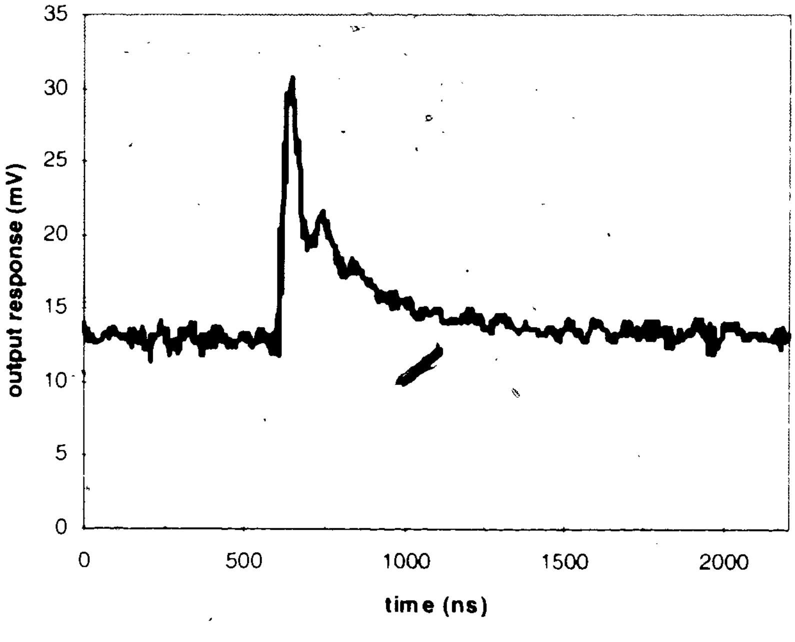

Figure 4.6 Output response of MSGC operated with Ar/CO_2 gas when V_c = -630V and V_d = -1000V

The longer falling time can also be caused by operating the QPA02 amplifier with larger load resistance. Figure 4.7 shows the temporal shape of the avalanche amplification signal of the MSGC which was operated under the same conditions as that in Figure 4.5, i.e. Vc = -700V, and Vd = -2000V, corresponding to a drift field of about 6700V/cm. The QPA02 was biased in the same conditions except the oscilloscope was in 1MΩ input impedance mode. The falling time increased to ~ 100ns while the rising time was still ~50 ns. Due to the very high load resistance, the pulse amplitude doubles.

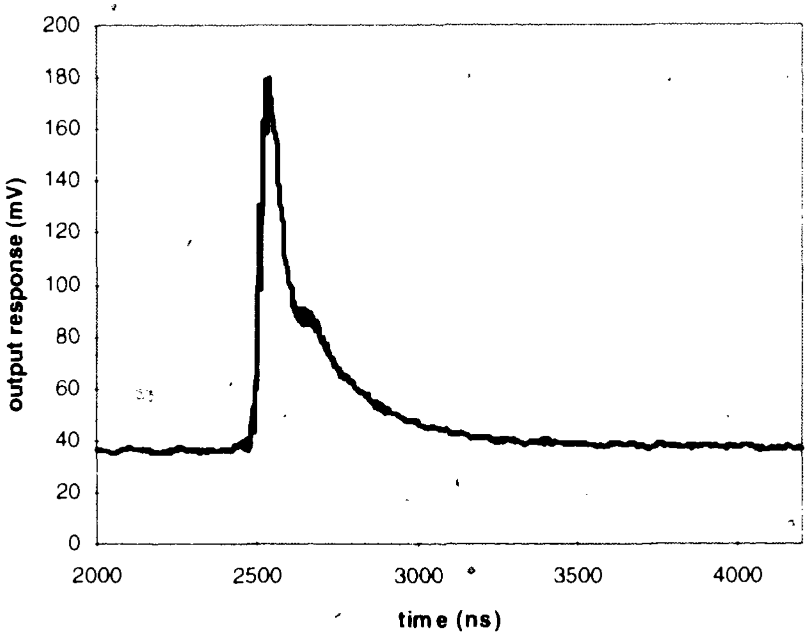

Figure 4.7 Output response of MSGC operated with Ar/CO$_2$ gas when the load resistance of QPA02 is 1MΩ

4.2.2 Signal amplitude vs. cathode voltage

The relation between the gain and the voltage field strength near the MSGC print was studied by varying the cathode voltage. Figure 4.8 displays the variations of output peak value as a function of the applied cathode potential for a fixed drift potential of -2000V.

Compared to the Ar/CO_2 gas, the MSGC had lower gain with the Ar/DME. Figure 4.9 displays the peak amplitude vs. cathode potential measured from the MSGC operating with the Ar/DME gas. The pulse amplitude was about half that of the MSGC when running with the Ar/CO_2 gas.

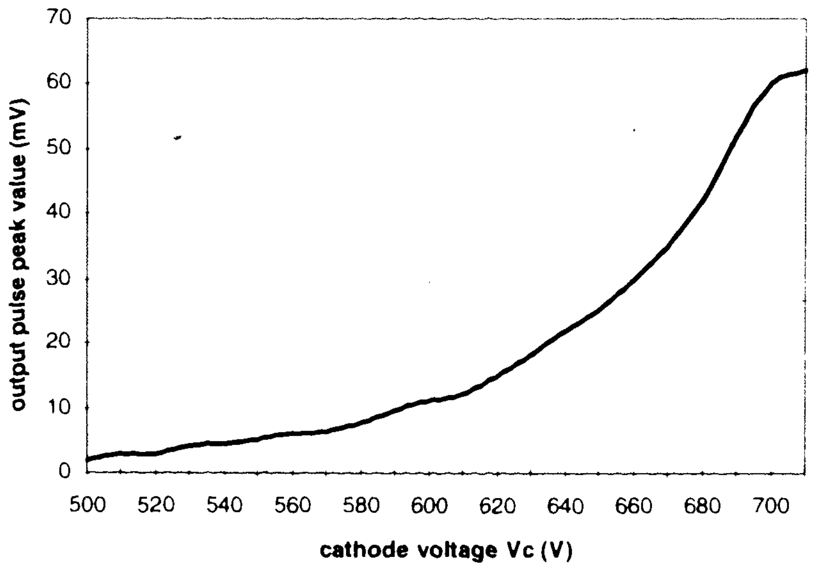

Figure 4.8 Relation between output pulse height and cathode voltage when MSGC was operated with Ar/CO_2 gas

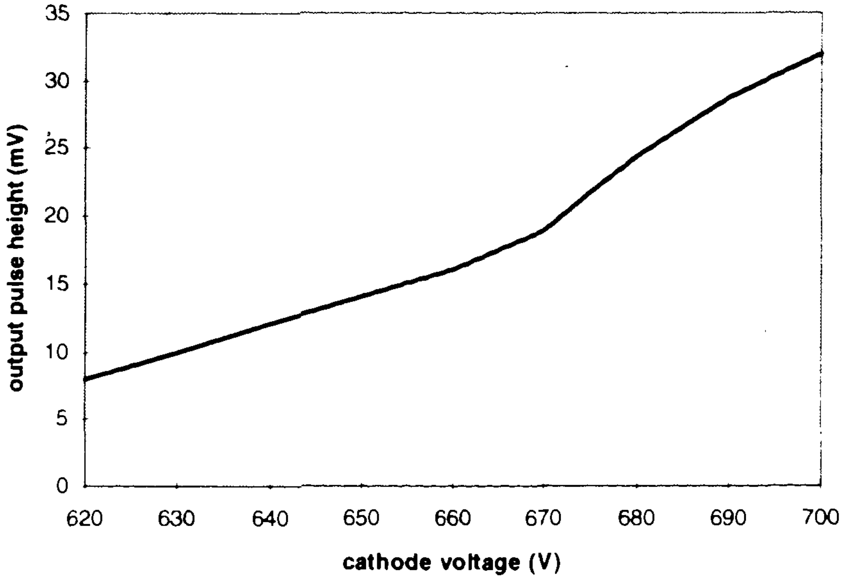

Figure 4.9 relation between output peak height and cathode voltage when MSGC was operated with Ar/DME gas

4.2.3 Pulse amplitude Vs drift voltage

The impact of the drift field on the gain of the MSGC was also studied. During this testing, the anode was grounded through a 1MΩ resistor while the cathode was supplied a voltage of -700V. The amplitude variation of collected electrical impulses at the anode was observed by changing the drift voltage. The amplitude of signals from anode stripes, as a function of the drift voltage, is plotted in Figure 4.13.

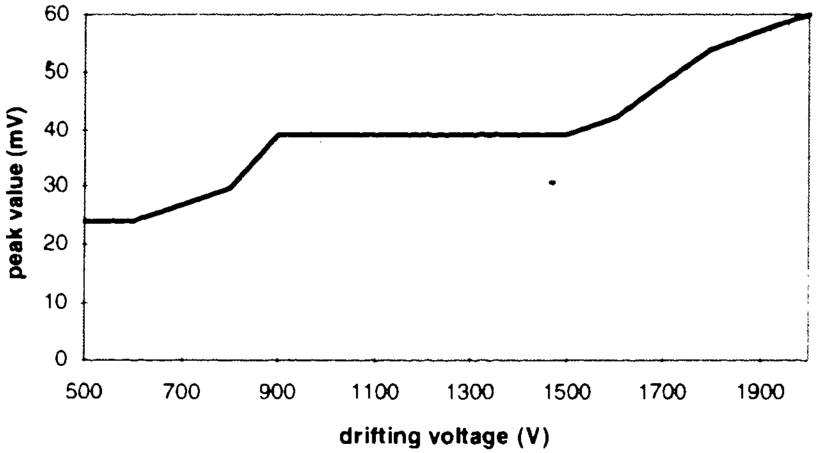

Figure 4.10 Curve of output pulse height Vs drift voltage when MSGC was operated with Ar/CO_2 gas when Vc = -700V

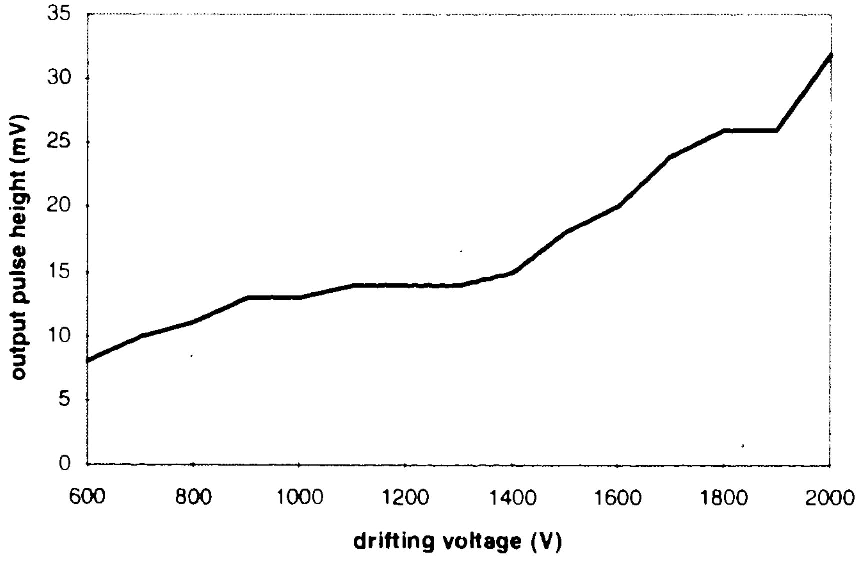

Figure 4.11 Curve of output pulse height Vs drift voltage when MSGC is operated with Ar/DME gas when Vc = -700V

Figure 4.11 shows the curve of output pulse amplitude vs. the drift voltage of the MSGC detector operated with the Ar/DME gas.

4.2.4 Temporal stability of MSGC

As discussed in Chapter 2, the avalanche discharge occurs in the vicinity of the dielectric substrate in the MSGC. This is one of the main disadvantages of the MSGC: the gain variation due to the accumulation of positive avalanche ions on the dielectric substrate limits the high rate capability of the detector. It has been reported that the gain of some MSGC detectors will drop and even stop working after operating for only 20 minutes at moderate x-ray fluxes. In our experiments, a conductive nickel oxidation layer was deposited on the surface of the MSGC print to remove the accumulated charge.

In order to see how the gain depends on the avalanche charge received and the effectiveness of the nickel layer on removing accumulated charge, the detector was illuminated during a day with the Fe^{55} radiation source. The activity of the Fe^{55} source was 100mCi. Figure 4.12 shows the variation of peak amplitude over one day. The gain of the MSGC is quit stable. It shows the gain variation was less than ±15% over 24 hours, indicating that the charge accumulating on the surface of the MSGC print was completely removed by the nickel conductive layer at these moderate X-ray fluxes.

It should be mentioned that aging phenomena can also be caused by the polymerization of gas molecules in the avalanche process. This causes a permanent damage in the electrodes since the polymeric compounds are fixed to the anodes and cathodes stripes.

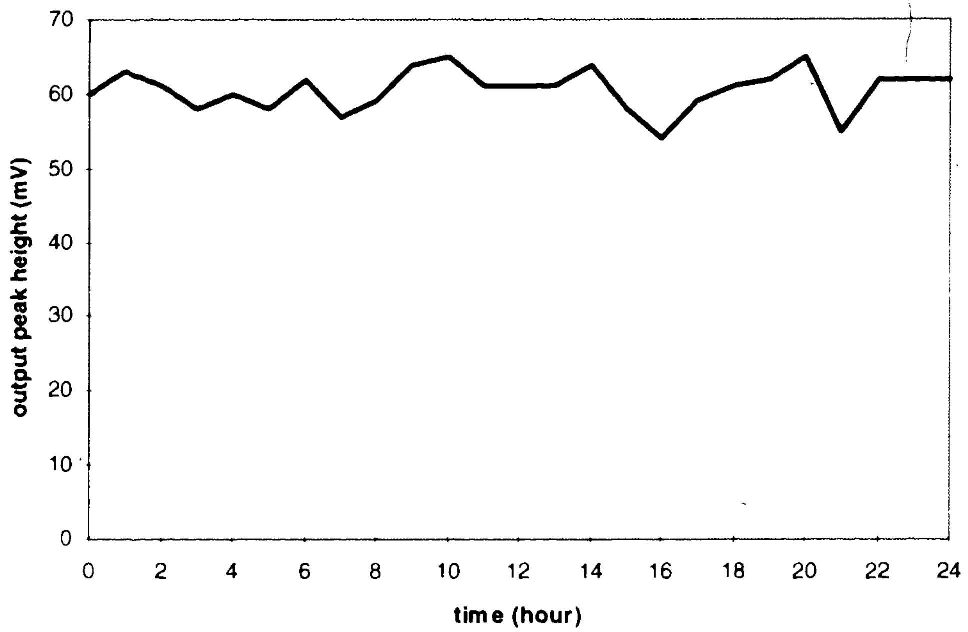

Figure 4.12 Variation of output peak height of MSGC over one day

4.2.5 Discharge damage

In the measurements reported above, the anodes were kept at ground potential and cathodes were set at negative voltage. A voltage of - 2000V was applied to the drift electrode. A stable signal, without discharge or any type of mechanical damage of the microstrip was observed when the cathode voltage was kept below -750V.

During the operation of the MSGC, often minor streamers develop. Normally, these streamers do not lead to a trip of the cathode power supply. However, since the heat capacity of a strip 1μm thick is very limited, damage by the melting or even evaporation of the anode strip can easily occur because a substantial amount of electrical energy is stored in the capacity of the cathode stripes. Figure 4.14 shows an example of a strip destroyed by such discharge when the applied voltage between anode and cathode was over 900V.

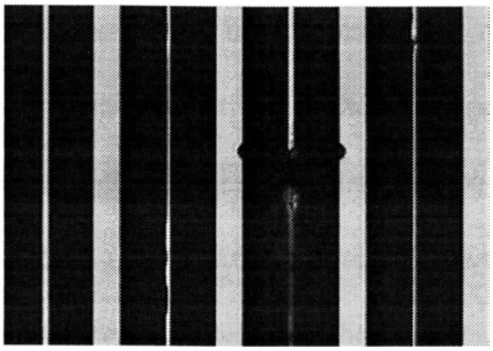

Figure 4.14 Damage of MSGC print by discharge

Normally, the streamer is terminated when the electric current has decreased below a certain limit. The end of the streamer can thus be eliminated by increasing the impedance of either the cathode or the anode strip, leading to an important reduction of the heat deposited.

4.3 Summary

To avoid the gain instability of the MSGC caused by ion accumulation, a nickel oxide layer was deposited on the top of the MSGC print. To remove ions on the insulating substrate as well as to apply high voltage (600 V) to anode and cathode, the desired sheet resistivity of passivation layer should be in the range of 10^{11} - 10^{14} Ω / square.

The nickel oxide layer of high resistivity has been achieved with DC sputtering nickel deposition in oxygen ambient, associated with a post heating process. The fabrication process of the high resistivity nickel oxide film has also been described. The electric property and stability have been investigated. The results show that the post baking process can increase the sheet resistivity of the nickel oxide film by two orders or more. The nonlinear behavior of the nickel oxide film can also be converted to linear I-V characteristic by post-heating. Auger spectrometry results show that the nickel atoms on the passivation layer were oxidized completely in the post heating process by absorbing external oxygen molecules.

Chapter 5 Characterization of Nickel Film and Deposition Process

The ion accumulation usually occurs when the MSGC x-ray detector is operated with high x-ray flux detection, which causes local gas gain instability. The stability of gas gain of MSGC was observed over 24 hours, as described in chapter 4. Limited by the availability of the radiation source, the experiments have only been conducted with an ^{55}Fe x-ray source of 100μCi intensity. Further testing with high flux rate sources is essential to confirm the capability of the nickel oxide passivation film. Yet such testing is time consuming and difficult to do.

Additionally, the properties of thin films depend strongly upon the deposition technique and conditions used. In order to achieve the desired film, optimum deposition conditions have to be found by carrying out experiments in a trial-and-error fashion with varying parameters. Furthermore, many of the parameters, such as background oxygen levels, are very hard to control, and are often deposition system dependent. This is especially true for film deposition processes using a cold plasmas because of the poor understanding of the mechanisms. Previous work [17] on the nickel oxide films has proved difficult to reproduce the passivation layer due to such system sensitivity of sputtering process. By introducing new measurements to observe and new methods to test the film, better control of the process can be obtained.

In this chapter, a new approach using scanning electron microscopy (SEM) is proposed to examine the capability of the nickel oxide passivation film to remove accumulated ions. An intense incident electron flux can be achieved by increasing the current of electron gun in a scanning electron microscope. By observing the charging effect in the SEM image, the capability of the MSGC for high flux x-ray detection can be tested.

It is known that the interaction of the oxygen with the nickel is a critical factor in the sputtering process of nickel oxide deposition. It can be expected that the characteristics of this reaction would be reflected by the spectrum and colour of the plasma glow. To enhance control of the sputtering deposition process, a real time monitoring system, which consist of a colour CCD camera, image board and a host computer, has been employed to analyze the plasma status.

5.1 Testing the performance of passivation film with the Scanning Electron Microscope

5.1.1 Charging up in Scanning Electron Microscopy

In SEMs, surface information is obtained by detecting the secondary electrons excited by bombardment of incident electrons. The incident electrons can be affected by the electrical field in the surroundings of the specimen, which will cause the image information to be dependent on the environmental condition. To avoid that, the specimen is usually required to be conductive, and tied at a constant voltage potential when the electron energy is above a few keV.

Under electron bombardment in the scanning electron microscope, an insulator can charge up, which will ruin the image. The degradation of SEM image is attributed to the electron accumulation on the insulating surface, which is similar to the situation occurring in a MSGC detection as described in chapter 1. Therefore, the ion accumulation of a MSGC can be simulated with the electron bombardment in scanning electron microscope, and the performance of the nickel oxide layer on elimination of ion accumulation can be tested by observing the SEM image of MSGC print.

5.1.2 Experimental procedure

The scanning electron microscope used in the experiment was an Autoscan of ETEC Corporation. A specimen less than 5mm by 5mm was cut from MSGC print, and glued in the sample post of the scanning electron microscope with silver conductive paste. The electrodes on the specimen of MSGC print were also connected to the post with silver conductive paste.

Three samples were made and tested. One was a specimen of the MSGC print without the nickel oxide passivation layer. The substrate of the MSGC was laboratory glass, which was of very high resistivity (over 10^{18} Ω/square). The second one was a specimen of the MSGC print with nickel oxide passivation film. The sheet resistivity of the passivation layer was 1.8×10^{13} Ω/square. To compare the behaviors of the MSGC prints with and without the nickel oxide passivation layer under the same irradiation condition, a specimen of the passivated MSGC print and a specimen of the unpassivated MSGC print were mounted side by side on one SEM sample post.

The chamber of SEM was pumped down to 10^{-3} torr. The specimen was illuminated by e-beam for 30 seconds before the electron accumulation was observed. During the observation, the scanning electron microscope was operated at 20 keV, and the current of electron gun was about 0.17 mA. The electron flux on the specimen surface was 1 mA/mm^2. As a comparison, suppose that the typical gas gain of the MSGC was 40000, the intensity of electron flux was equivalent to a radioactive source of 0.72 Ci over 1 mm^2 area, if the efficiency of ionization is 100%. An intensity of 0.72 Ci over 1 mm^2 is a very strong x-ray source, which is over the loading limit of copper target.

5.1.3 Results

The following aspects of nickel oxide passivation layer have been investigated with SEM: (a) observation of charging effect on the bare MSGC print substrate, (b) comparison between a coated MSGC print and an uncoated MSGC print under the same irradiated condition.

(a) Charging effect of the insulating MSGC substrate

Figure 5.1 shows the images of the uncoated and the coated MSGC prints. These two samples were tested under the same conditions. The SEM was still operated at 20keV and 0.17mA. The samples have been exposed to e-beam for 30 seconds before the

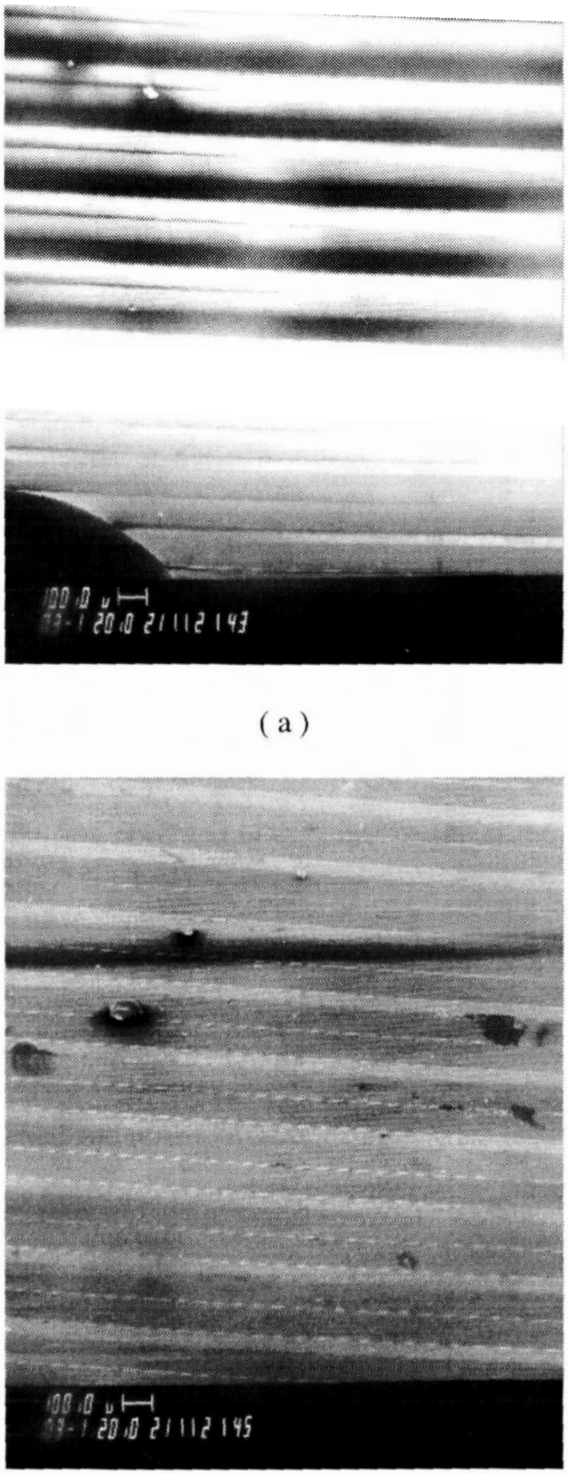

(a)

(b)

Figure 5.1 SEM images of (a) uncoated and (b) coated MSGC prints pictures were taken, which is equivalent to the 5.1×10^{-3} coul/mm^2. Due to the charging effect, the spatial resolution of the uncoated MSGC print was poor. Only a blurred image was obtained, as shown in Figure 5.1(a). Whereas, the edges of electrodes and other details can still be recognized from the image of the coated MSGC prints, as shown in Figure 5.1 (b). This indicated that the nickel oxide film could drain off the surface electrons effectively without accumulation.

For further examination of the performance of the nickel oxide film, the SEM images were observed after scanning a small area (2.56mm^2) for 30 seconds. Figure 5.2 (a) shows the test result for the uncoated MSGC film. It can be seen from Figure 5.2 (a) that there was a brighter square in the upper side, which indicated the heavier charging effect caused by long duration electron scanning. In contrast, there were no any bright areas due to electron repulsion observed in the SEM image of the coated MSGC print, as shown in Figure 5.2 (b)

(b) Comparison of the uncoated and coated MSGC prints

Although the coated and uncoated MSGC prints were tested by the same scanning electron microscope operated in the same condition, an attempt was made to avoid any fluctuations for a good comparison. To do this, the uncoated and coated MSGC prints were mounted in the same sample post of the scanning electron microscope, so that their images could be observed under the same irradiation condition. Figure 5.3 shows the image at the junction of the uncoated MSGC print and the coated MSGC print. The left side of the figure is the image of the coated MSGC print. The right side of the figure is

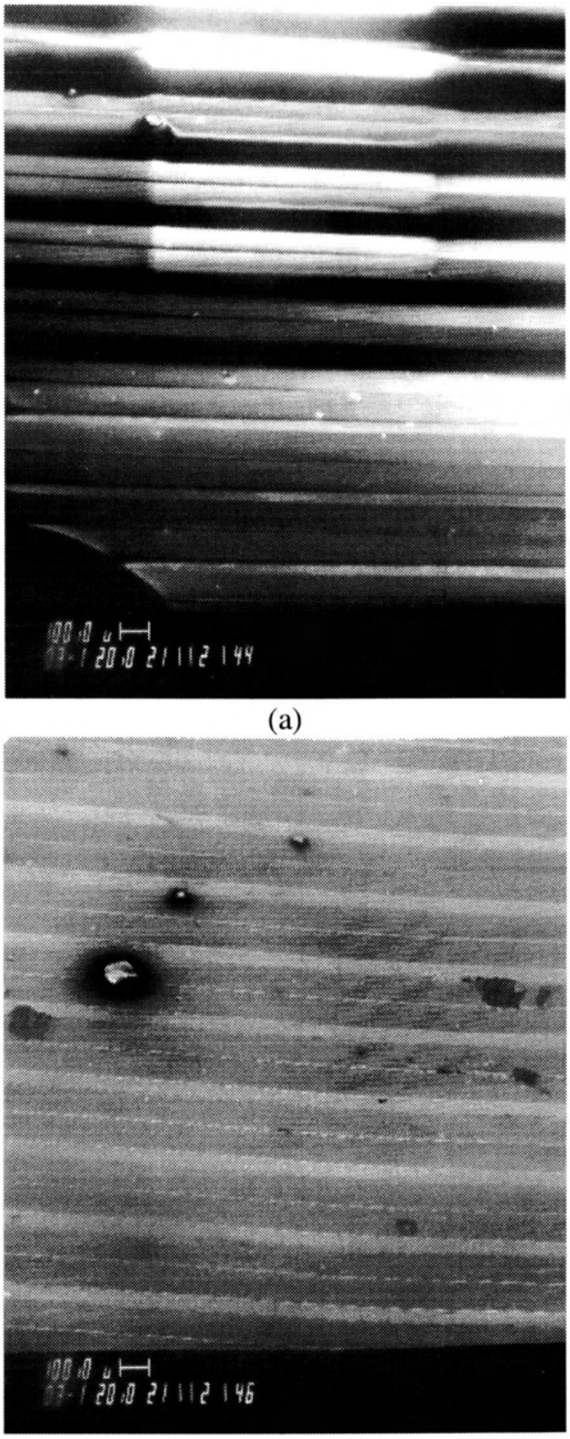

(a)

(b)

Figure 5.2 SEM images of the (a) uncoated and (b) coated MSGC prints after 30 seconds of electron scanning the image of the uncoated MSGC print. There was some silver conductive paste in the middle. The result shows that the coated MSGC print was not charging up under the electron bombardment. The detailed surface topography of coated MSGC print can be clearly seen from the image. Whereas, a bright image of the uncoated MSGC print was obtained, which was attributed to the charging on the uncoated side. The reason that both the anodes and cathodes were visible was that all the electrodes were grounded through the sample post.

Figure 5.3 Comparison of SEM image of the coated and uncoated MSGC print

5.1.4 Summary

A new approach was proposed to examine the resistance to ion accumulation of a MSGC detector. In this method, a scanning electron microscope was employed to simulate the ion accumulation process using electron bombardment. The charging effect was tested by observing the spatial resolution of the SEM image. The experimental results showed that the nickel oxide passivation layer successfully removed the surface electrons under high irradiation rate, which is equivalent to 0.71 C/mm^2 radiation source. The charging up phenomena of the uncoated MSGC prints was observed easily. This was an indirect testing method. Nevertheless, it was a convenient way to test the MSGC prints, especially when there was no access to high intensity radiation sources and MSGC detection system.

5.2 Control of nickel sputtering deposition with colormetric monitoring

As noted in chapter 4, MSGC prints were successfully passivated with nickel oxide film. Although the system parameters on sputtering machine were found by trial and error, additional parameters in monitoring the sputtering deposition process have been investigated.

The proprieties of the fabricated thin film is highly dependent on the plasma status generated between the target and substrate. Therefore plasma diagnostic techniques are important to determine the plasma conditions. The diagnostic methods themselves should not disturb the plasma. In this thesis, the plasma for nickel film sputter deposition was monitored by measuring the emission light of the plasma with a colour CCD imaging system. The imaging system also has the potential of monitoring the variation of plasma in time and space.

5.2.1 Plasma and sputtering process

The nickel film sputtering deposition was carried out in a cold plasma. To remain ionized, the gas must receive constant inputs of energy to offset the recombination of the charged particles in it. It must also be kept at low pressure (~ 10^{-3} torr), to reduce the collision rate and thus the recombination rate of the ions. Plasmas for nickel film deposition are formed by applying a DC electric field to argon gas held at a low pressure in a vacuum chamber.

Spectrophotometric measurement, however, may involve elaborate and expensive instruments, although the results are available in a perfectly definite and unambiguous form. The alternative is to monitor the plasma in several components. A system for optical measurement is schematically shown in Figure 5.4. In this system a colour camera is employed to capture the colour information of the plasma glow. The data are digitized by a image board and processed in a personal computer. Obviously, this system is able to in site monitor the plasma conditions in terms of chromacity, with which the spatial and temporary information of plasma can also be obtained.

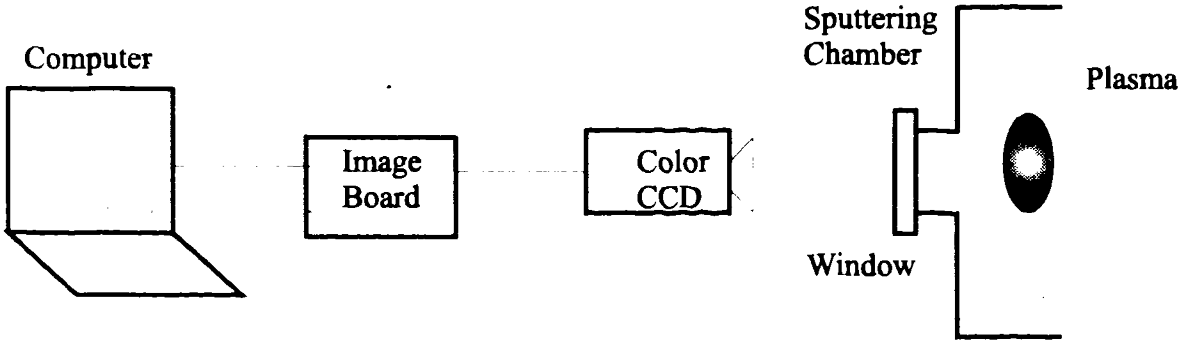

Figure 5.4 Schematic diagram of the system for chromacity measurement

5.2.3 Camcorder measurement of plasma

A proof of concept experiment for monitoring the sputtering deposition process has been conducted. A Panasonic colour Camcorder was used to record the chromatic information of the plasma glow. The RGB components of colour video signals were separated and digitized by a image board, and processed in a PC.

The colour Camcorder captured the colour image with a CCD detector array. Each pixel consisted of three detection elements with different colour filters, *(R)*, *(G)* and *(B)*. The three primaries of this chromaticity measurement system were the colour of the three filters, (R), (G) and (B). Their chromacitiy coordinates could be determined by their spectral transmission curves.

The colour images of plasma glow in different gas ambient were acquired, recorded on tape and digitized by the image card. Figure 5.5 shows the typical pictures of plasma flames. When only pure argon was in sputtering chamber, the plasma glow was a bluish white. When oxygen was introduced ranging from 5:1 argon/oxygen to 1:1 argon/oxygen, the plasma glow overall became redder with increasing oxygen.

The relative compositions of each plasma glow were calculated. The colour of plasma glow was known to change from blurish white to pink when the oxygen flow rate increases, the ratio of *r* to *b* was chosen as the criterion for monitoring the gas ambient in the sputtering chamber. Two methods were used to calculate the *r*/*b* ratio of the plasma flames: first, the plasma glow region was determined based on the light intensity. Then the central point of the region was selected to calculate the *r*/*b* ratio. Second, a central row in the image of the plasma glow was selected. The average r/b ratio along this row was calculated.

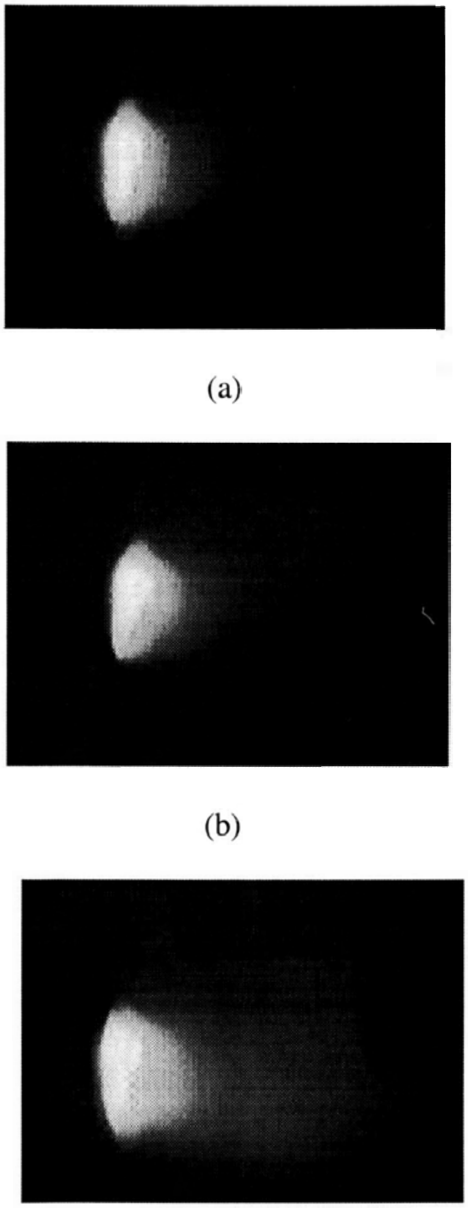

(a)

(b)

(c)

Figure 5.5 Images of the plasma glow under (a) pure argon (b) 5:1 argon/oxygen (c) 1:1 argon/oxygen

In the experiments, data of the plasma glow was acquired under three gas conditions, i.e. pure argon, 5:1 argon/oxygen ratio and 1:1 argon/oxygen ration. After changing the gas flow rate, the plasma reaction was allowed to get stable for 10 minutes before the measurement. The experimental results are listed in table 5.1. It shows that the *r/b* ratio decreased when the oxygen flow rate increased. It indicates that colour of the plasma glow was moving toward the red from blue, which was consistent with the observation of plasma glow colour. Quantitative indication was given by the measurement, and about two times difference existed in the average *r/b* ratio when argon/oxygen ratio was 1 compared with pure argon. A larger difference was found in the central point measurement.

The changing of plasma glow, which was caused by introducing oxygen gas, also implied that the oxygen molecules were ionized in the plasma, and became very active ions. It can be predicted that a chemical reaction between oxygen and nickel atoms is necessary to form the nickel oxide deposited on the surface of MSGC prints. Although not all nickel atoms need to be oxidized completely, it plays a critical role in the conversion of nickel/nickel oxide film to the high resistivity passivation layer by the post baking process. As noted in chapter 4, it was found that the $10^{14}\Omega$/square sheet resistivity could not be achieved from a metallic nickel thin film with a post baking process of as high as 500°C temperature.

Table 5.1 Experimental results of measurement of plasma glow

	central point			central row		
gas condition	r/b	r/g	g/b	r/b	r/g	g/b
pure argon	1.23	0.18	6.83	1.58	0.17	9.29
5:1 Ar/O_2	3.56	0.14	25.43	2.35	0.13	18.08
1:1 Ar/O_2	12.48	0.19	65.68	5.36	0.17	31.53

5.2.4 Computer-Camera measurement of plasma

Several computer-based live video camera systems have become available which avoid the need for the frame grabber. A monitoring system was built up with a CCD camera connected through the parallel port of a PC. Since the image board was not required in this system, the cost of the monitoring system drops significantly. We used a QuickCam® color CCD camera of 240×240 pixels, which costs only Cnd$350.

In this measurement, the camera was rigidly mounted on a stand so the same location in the plasma stream could be measured from frame to frame. Also the real time control of the CCD exposure level allowed both the brighter and dimmer areas of the plasma to be investigated. 256 levels were taken for each r, g, b colours. As a comparison, two sets of the plasma images were acquired, corresponding to the pure argon sputtering chamber and 1:1 argon/oxygen sputtering chamber. To investigate the different parts of the plasma, the images of the plasma glow were taken by using different exposure levels to image the different parts of the plasma beam. Figure 5.6 shows the images of the plasma glow of the pure argon chamber while Figure 5.7 shows the images of the plasma glow of the 1:1 argon/oxygen chamber.

The spatial variations of the plasma colour was studied in this experiment. 12 points on the scene were selected to calculate the chromaticity coordinates of the glow. Figure 5.8 shows the positions of the sampling points.

Table 5.2 and 5.3 list the raw data of the chromatic measurement. The ratio of red and blue components was still used as the criterion, and the experimental results, which were calculated from Table 5.2 and 5.3, are listed in table 5.4 and table 5.5. The point index used in those tables is shown in Figure 5.8. It was defined as under exposure when the value of any component was less than 50, while it was defined as over exposure when the value of any component was equal to 255. " - " in Table 5.4 and 5.5 indicates that the CCD camera was operating in either under exposure condition or over exposure condition.

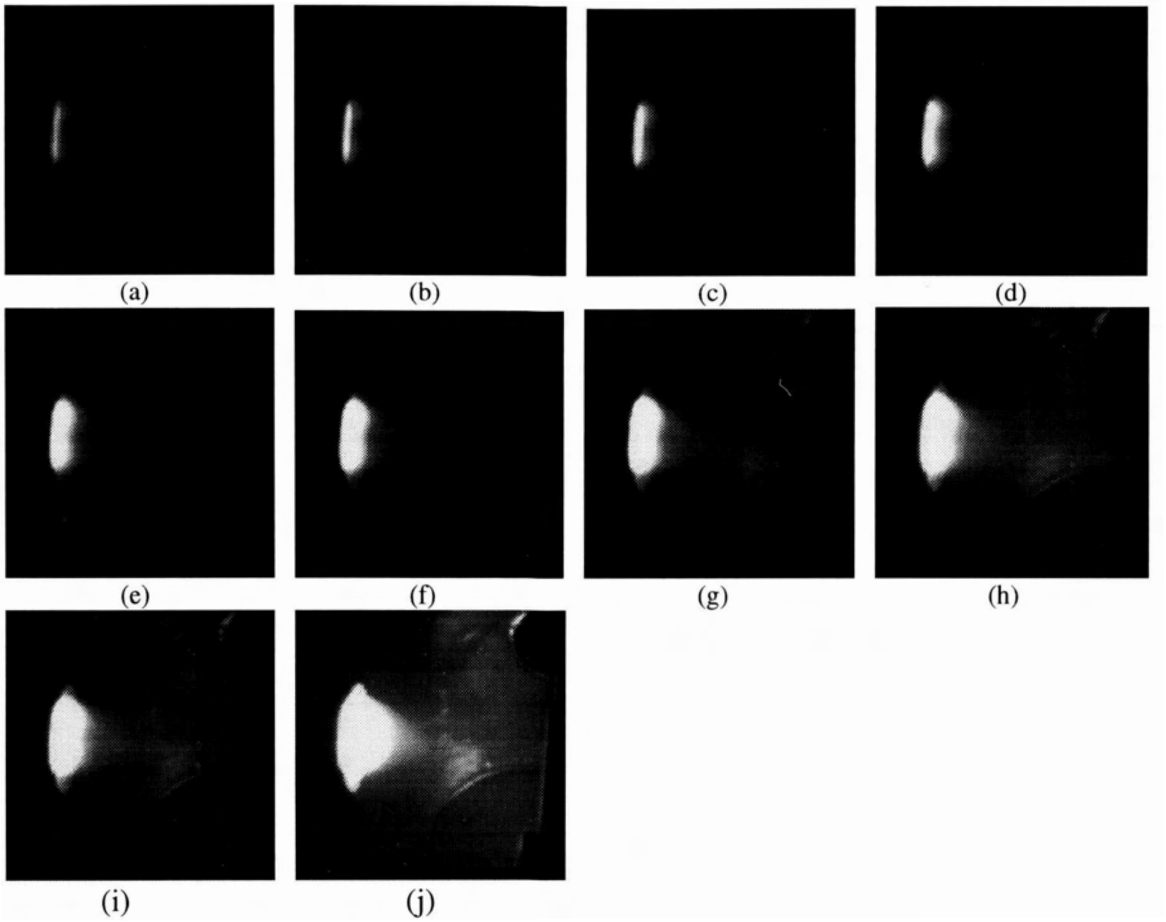
(a) (b) (c) (d) (e) (f) (g) (h) (i) (j)

Figure 5.6 The plasma image set for the pure argon chamber under different illumination setting of camera
(a) 110, (b) 120,(c) 130, (d) 140, (e) 150, (f) 160, (g) 170, (h) 180, (i) 190 (j) 200

From the experimental results listed in table 5.4 and table 5.5 it can be seen that the ratio of red and blue components increased about 30% when the equal quantity of oxygen was introduced into the pure argon sputtering chamber. Obviously, the r/b ratio increased when some oxygen was introduced into the sputtering chamber, which is consistent with our previous analysis and experimental results. It can also concluded that the different illumination of the CCD camera should be set to observe the spatial distribution of the plasma chromacity. Table 5.6 lists the ratio between each item of Table 5.4 and the corresponding item in Table 5.5.

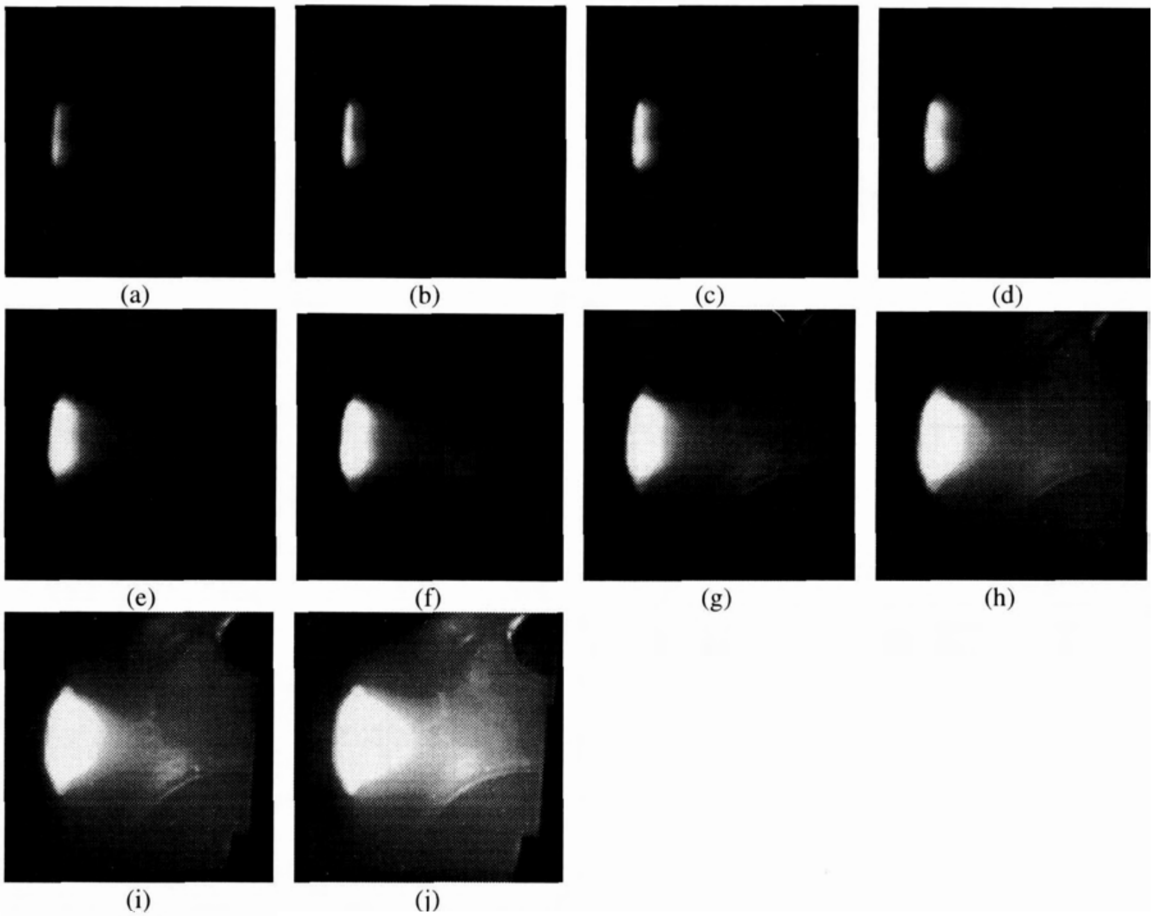
(a) (b) (c) (d)
(e) (f) (g) (h)
(i) (j)

Figure 5.7 The plasma glow image set for the 1:1 argon/oxygen chamber under different illumination setting of camera
(a) 110, (b) 120,(c) 130, (d) 140, (e) 150, (f) 160, (g) 170, (h) 180, (i) 190 (j) 200

Table 5.2 Experimental data of plasma chromatic measurement of pure argon chamber

position																	
illumination	r	g	b	r	g	b	r	g	b	r	g	b	r	g	b	r	g	b
110	3	0	0	3	0	0	9	7	2	122	115	157	0	0	0	1	0	0
120	2	0	0	3	1	1	12	6	6	255	193	255	4	1	0	0	0	0
130	2	1	2	4	4	5	18	9	6	255	255	255	1	0	0	4	1	0
140	8	5	5	9	7	3	22	15	18	255	255	255	7	5	0	3	5	0
150	14	12	9	18	12	15	35	27	27	255	255	255	11	12	5	9	9	4
160	17	17	21	20	21	16	46	41	38	255	255	255	17	15	17	15	14	11
170	31	29	29	36	36	36	73	66	65	255	255	255	29	26	32	28	24	21
180	50	49	53	58	55	58	109	110	104	255	255	255	39	42	46	44	40	41
190	69	72	83	84	84	97	255	155	159	255	255	255	57	63	70	61	64	66
200	110	107	125	138	136	141	255	245	241	255	255	255	95	101	113	98	92	97

Table 5.2 continued

position																	
illumination	r	g	b	r	g	b	r	g	b	r	g	b	r	g	b	r	g	b
110	9	2	0	95	92	121	0	1	0	0	0	0	4	0	0	2	0	0
120	8	2	3	255	157	199	0	1	0	0	0	0	6	0	0	3	0	0
130	9	6	3	255	219	255	3	1	2	0	0	1	8	1	0	1	1	0
140	15	10	4	255	255	255	6	6	5	4	2	0	6	3	1	4	4	0
150	20	16	9	255	255	255	11	10	5	7	7	0	9	4	0	4	3	5
160	29	24	23	255	255	255	13	15	20	9	8	10	11	8	5	8	9	5
170	41	36	31	255	255	255	26	23	25	15	17	22	20	12	18	14	16	13
180	63	59	61	255	255	255	44	42	49	29	27	29	31	22	24	25	22	26
190	93	89	87	255	255	255	60	61	64	44	40	45	44	35	40	40	37	44
200	144	146	142	255	255	255	102	95	109	63	64	71	58	50	59	58	53	64

Table 5.3 Experimental data of plasma chromatic measurement of 1:1 argon/oxygen chamber

position																		
illumination	r	g	b	r	g	b	r	g	b	r	g	b	r	g	b	r	g	b
110	4	3	4	5	2	5	14	9	8	143	127	213	0	0	0	0	0	0
120	5	1	2	6	2	1	21	11	5	255	201	255	0	0	0	8	4	2
130	11	6	1	11	7	10	30	19	14	255	255	255	8	3	6	9	5	4
140	17	10	10	20	13	10	43	28	24	255	255	255	9	7	2	13	8	8
150	23	19	23	32	24	33	64	44	52	255	255	255	21	16	21	23	19	17
160	35	26	29	43	35	41	89	64	61	255	255	255	30	24	25	33	22	28
170	60	43	49	74	56	64	146	104	103	255	255	255	51	37	48	57	39	47
180	86	67	77	114	87	100	255	166	165	255	255	255	76	58	75	85	65	71
190	138	102	122	171	133	143	255	249	254	255	255	255	113	92	107	125	96	113
200	255	161	189	255	210	239	255	255	255	255	255	255	183	144	167	203	156	174

Table 5.3 continued

position																		
illumination	r	g	b	r	g	b	r	g	b	r	g	b	r	g	b	r	g	b
110	0	0	0	100	87	144	0	0	0	0	0	0	0	0	0	0	0	0
120	8	2	8	152	148	210	4	2	1	0	0	0	0	0	0	0	0	0
130	21	10	8	255	217	255	8	6	5	5	2	2	0	0	0	0	0	0
140	29	17	15	255	255	255	14	6	4	8	5	6	16	8	3	8	2	1
150	43	28	29	255	255	255	15	14	20	16	13	13	20	12	15	11	6	10
160	60	43	43	255	255	255	26	20	19	21	16	18	26	17	13	17	14	15
170	95	71	70	255	255	255	43	31	40	35	26	27	40	24	31	27	19	23
180	143	107	113	255	255	255	69	51	63	55	43	48	59	42	45	42	31	40
190	255	166	167	255	255	255	103	82	103	83	65	81	88	63	66	65	45	61
200	255	246	255	255	255	255	163	126	155	129	100	131	134	98	108	99	73	90

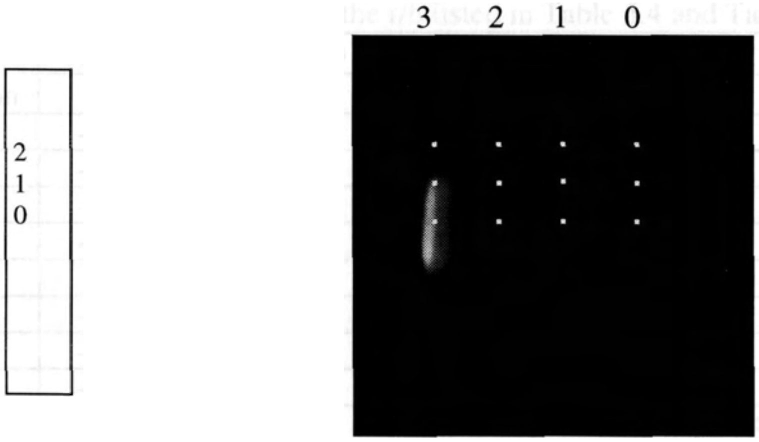

Figure 5.8 Sampling points on the image of plasma glow

Table 5.4 Experimental results of the multiple point chromatic detection
(pure argon chamber)

position	0,0	1,0	2,0	3,0	0,1	1,1	2,1	3,1	0,2	1,2	2,2	3,2
illumination	r/b ratio											
110	-	-	-	-	-	-	-	-	-	-	-	-
120	-	-	-	-	-	-	-	-	-	-	-	-
130	-	-	-	-	-	-	-	-	-	-	-	-
140	-	-	-	-	-	-	-	-	-	-	-	-
150	-	-	-	-	-	-	-	-	-	-	-	-
160	-	-	-	-	-	-	-	-	-	-	-	-
170	-	-	1.12	-	-	-	-	-	-	-	-	-
180	-	-	1.05	-	-	-	-	-	-	-	-	-
190	0.83	0.87	-	-	0.81	0.92	1.07	-	0.94	-	-	-
200	0.88	0.98	-	-	0.84	1.01	1.01	-	0.94	0.9	0.98	0.91

Table 5.5 Experimental results of the multiple point chromatic detection
(1:1 argon/oxygen chamber)

position	0,0	1,0	2,0	3,0	0,1	1,1	2,1	3,1	0,2	1,2	2,2	3,2
illumination	r/b ratio											
110	-	-	-	-	-	-	-	-	-	-	-	-
120	-	-	-	-	-	-	-	-	-	-	-	-
130	-	-	-	-	-	-	-	-	-	-	-	-
140	-	-	-	-	-	-	-	-	-	-	-	-
150	-	-	-	-	-	-	-	-	-	-	-	-
160	-	-	1.46	-	-	-	-	-	-	-	-	-
170	-	1.16	1.42	-	-	-	-	-	-	-	-	-
180	1.12	1.14	-	-	-	1.20	1.27	-	-	-	-	-
190	1.13	1.20	-	-	1.06	1.11	1.53	-	1.26	1.02	1.33	1.07
200	-	-	-	-	1.10	1.17	-	-	1.29	0.98	1.24	1.1

Table 5.6 ratio between the r/b listed in Table 5.4 and Table 5.5

position	0,0	1,0	2,0	3,0	0,1	1,1	2,1	3,1	0,2	1,2	2,2	3,2
illumination.	variation of r/b ratio											
110	-	-	-	-	-	-	-	-	-	-	-	-
120	-	-	-	-	-	-	-	-	-	-	-	-
130	-	-	-	-	-	-	-	-	-	-	-	-
140	-	-	-	-	-	-	-	-	-	-	-	-
150	-	-	-	-	-	-	-	-	[illegible]	-	-	-
160	-	-	-	-	-	-	-	-	-	-	-	-
170	-	-	1.27	-	-	-	-	-	-	-	-	-
180	-	-	-	-	-	-	-	-	-	-	-	-
190	1.36	1.38	-	-	1.31	1.21	1.43	-	1.34	-	-	-
200	-	-	-	-	1.31	1.16	-	-	1.37	1.09	1.27	1.21

5.2.5 Summary

A measurement technique was developed to control the nickel oxide passivation process. A monitoring system, which consisted of a colour CCD camcorder, an image board and a host computer, was employed to monitor spectral components of the plasma glow in site. Due to the CCD detector array used in the measurement, the system has potential to acquire 2 dimensional chromatic information in real time.

The ratio of *r* and *b* was chosen as the criterion of monitoring the plasma condition. Experimental results show that the average r/b ratio can be changed by two times when percentage of oxygen in chamber was increased from 0% to 50%.

The monitor system, alternatively, was also built up with a QuickCam connected to the serial port of a PC. The advantage of this system was that the image board was avoided so that the overall cost of the monitoring system decreased significantly. Experimental results shows that the r/b ratio increased as much as 40%, which can be used as the criterion to monitor the plasma status.

Chapter 6 Conclusions and Future Works

In this thesis MSGC prints have been fabricated with basic photolithographic processes. To avoid charge accumulation on the insulating substrate under high flux, the MSGC prints were passivated with a nickel oxide film by sputtering deposition. The desired sheet resistivity of the passivation layer was achieved by controlling the gas ambient in sputtering chamber and a post baking process, which resulted in values in the range of $10^{11} \sim 10^{14}$ Ω/square.

The characteristics and properties of the nickel oxide film have been investigated. The V-I curves of the nickel oxide film were measured with a semiconductor parameter analyzer. It has been found that the nickel oxide film performs linear I-V relation after the post baking process. Stability of nickel oxide film has also been examined by observing the variation of the sheet resistivity for a long period. The results showed that the sheet resistivity of the nickel oxide film is always in the desired range, and became stable after one week.

A MSGC x-ray detection system has been assembled to test the performance of the MSGC prints in x-ray radiation detection. Gas gains over 10^4 were achieved with the MSGC prints when anode-cathode voltage was -700V and drift voltage was -2000V. The pulse width is around 100 ns, which implies that the MSGC detection system can be operated up to the 10 MHz.

To improve the reproducibility of the nickel oxide passivation process, a chromatic monitor system was introduced into the sputtering process. The plasma status and the gas ambient in the sputtering chamber were characterized by monitoring the emission light of the plasma flame. Preliminary experimental results showed that the variation of oxygen gas flow rate could be sensed by the monitor system.

In this thesis, a novel approach was proposed to verify capability of the nickel oxide film to eliminate the ion accumulation on the insulating substrate. When the MSGC prints were observed under SEM, electrons from the SEM also cause the insulating substrate charging up, and lead to a blurred image. By observing the SEM image of the MSGC prints, one can tell whether those electrons hitting the MSGC print surface could be drained by the nickel oxide film.

For further investigation, the following studies are suggested:

(1) The performance of the nickel oxide film should be verified under high intensity X-ray radiation;

(2) SEM results should be compared with intense X-ray flux results;

(3) The colour CCD camera should be calibrated before being used in a chromatic monitoring system.

Before a X-ray detection system using MSGCs can be used in industrial applications, it is suggested that further experiments and improvements should be conducted, which include wiring the MSGC prints, adding a high speed pulse counter to the system, and selecting a working gas mix.

(1) wiring the MSGC prints

To achieve high spatial resolution and high gain the anode pitch of the MSGC prints is about 200 ~ 400 μm. Therefore, a high density wiring method should be used to connect each electrode to its preamplifier.

(2) high speed pulse counter

The MSGC x-ray detection system measures the radiation intensity by counting the number of the pulses caused by x-ray photons. A high speed pulse counter should be used to process the signal from the preamplifier of each channel. The bandwidth of the counter should be large enough to record the pulses of 100ns width.

(3)selecting working gases

More efforts should be exercised in selecting working gases for the MSGC because chemical contamination has already been found in the MSGC prints. Various ionization gases should be tested in terms of both gas gain and chemical stability. From previous research of other groups, Ar:DME may be a good choice .

References

1. A. G. Michette and C. J. Buckley, *X-ray Science and Technology*, Institute of Physics Publishing, 1993
2. G. Charpak, *Reviews of Modern Physics*, **65**, 591(1993)
3. Oed, et al, *Nucl. Instr. and Meth.*, **A263,** 351(1988)
4. P. Rice-Evans, Spark, *Streamer and Proportional Drift Chamber*, The Richelien Press, 1974
5. C. F. Hendee, S. Fine, and W. B. Brown, *Review Sci. Instrum.*, **27**, 531(1956)
6. G. Charpak, R. Bouclier, T. Bressaui, J. Favier and C. Zupancic, *Nucl. Instrum Meth.*, **62**, 202(1968)
7. Bouclier et al., *Nucl. Instrum. Meth.*, **A323**, 240(1992)
8. S. Brons, W. Bruckner, M Heidrich, I. Konorov and S. Paul, *Nucl. Instrum Meth.*, **A342**, 411(1994)
9. Angelini et al, *Nucl. Instrum. Meth.*, **A315**, 21(1992)
10. Bouclier, M Capeans, C Garabatos, G. Manzin, G. Million, L. Ropelewski, F. Sauli, E. Shefer, L. Shekhtman, T. Temmel, G. Della Mea, G. Maggioni, and V. Figato;

Proceeding of the International Workshop on Micro-Strip Gas Chambers, Legnaro 13 (1994)

11. M. Salomon, J. Armitage, G. Chapman, et al, *Nucl. Instru. Meth.*, **A351**, 313(1994)

12. Pestov Yu, and L. I. Shekhtman, *Nucl. Instr. and Meth.*, **A338**, 368(1994)

13. J.J. Florent, J. Gaudaen, L. Ropelewski and F. Sauli, *Nucl. Instr. and Meth.*, **A329**, 125(1993)

14. F. Angelini et al, *Nucl. Instr. and Meth.*, **A283**, 755(1989)

15. F. Ortuo-Prados and C. Budtz-Jorgensen, "A study of surface treated MS-plates", *International Workshop on Micro-Strip Gas Chambers*, 159(1994)

16. J. Dubeau et. al, *Nucl. Instr. Meth.*, **A267**, 177(1995)

17. R. Bouclier, G. Million, L. Ropelewski, F. Sauli, Yu N. Pestov and L. I. Shekhtman, *Nucl. Instr. Meth*, **A332**, 100(1993)

18. S. C. Taylor et. al, *IEEE Trans. Nucl. Sci.*, **42**, 432(1995)

19. T. Zimmerman, *IEEE Trans. Nucl. Sci.*, **37**, 439(1990)

20. Lab Instruction of ENSC451, School of Engineering Science, Simon Fraser University, 1995

Appendix 1 QPA02 Amplifier

The output electrical signals from MSGC are amplified, measured and displayed with the readout electronic system. The readout electronic system consists of a QPA02 amplifier and the Tektronix 2025 digital storage oscilloscope. The QPA02 is a high speed bipolar transresistance charge amplifier. It converts an impulse of electric charge to a fast voltage pulse. It was originally designed as a silicon strip amplifier in Fermi Lab. The gain of QPA02 was claimed in the order of 15mV/fC while the rise time was less than 38 ns.

A1.1 Schematic of QPA02 amplifier

The QPA02 is a two stage amplifier. The schematic of QPA02 is shown in Figure A1.1. The first stage is a transresistance feedback amplifier in common emitter configuration to convert a charge input to a voltage output. In this stage, Q1 is input transistor in common emitter configuration. The cascade transistor Q2 limits input capacitance due to Miller effect. The transistor Q3 is a voltage follower, which buffers the output signal to the second stage. The second stage is a differential voltage amplifier. Its function is to boost the gain, shape the preamp output, and provide differential outputs

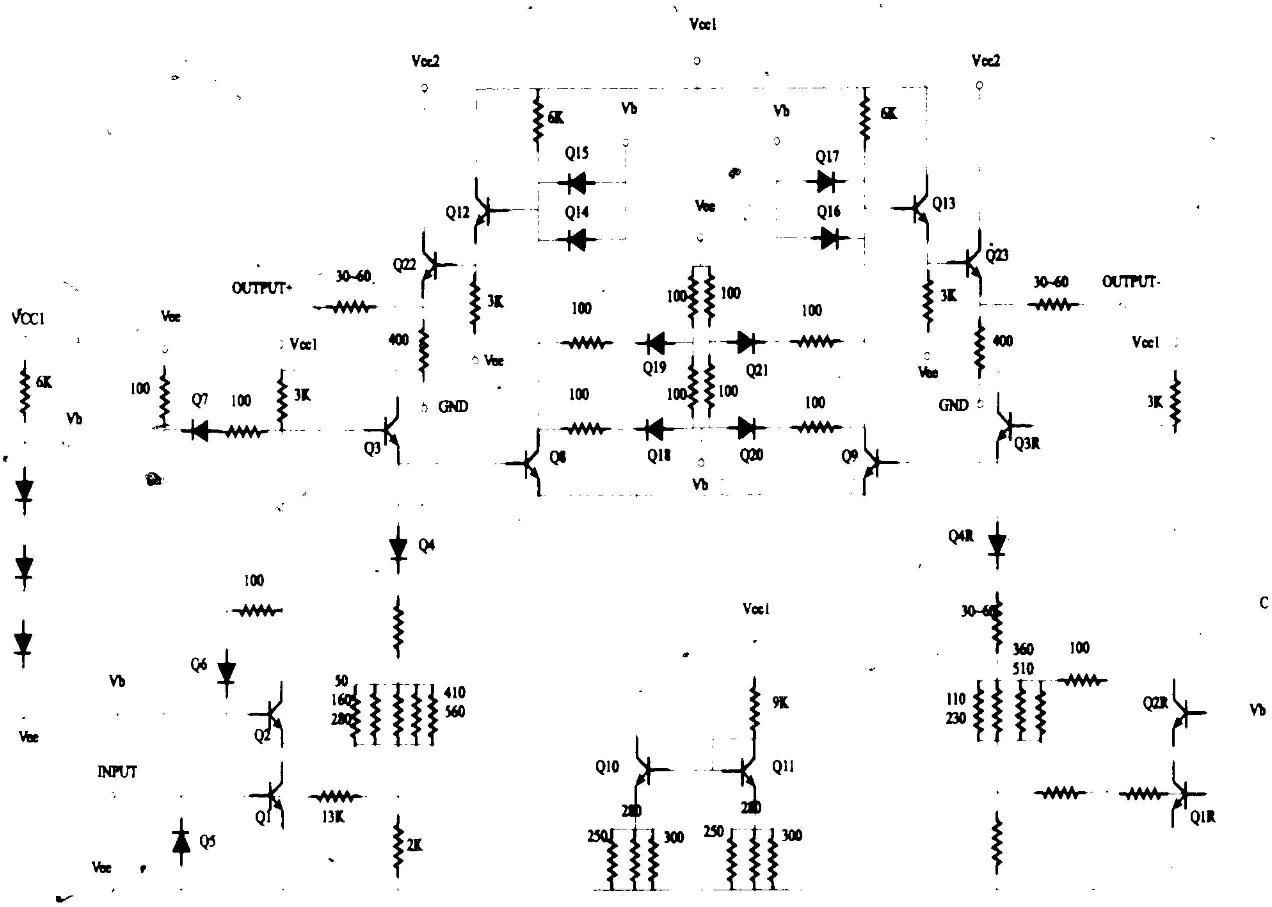

Figure A1.1 QPA02 schematic [28]

to drive a transmission line. A current mirror, Q10 and Q11 biased the differential pair, Q8 and Q9. A reference preamp stage, which is similar to the input stage, is connected to Q9 to provide DC tracking to the second stage. This reference can alleviate the fluctuation of the DC bias levels due to temperature effect while the gain of second stage is high. The amplified differential signal at the collectors is buffered by Q12, Q13, Q22 and Q23 so that a transmission line can be driven directly.

It can be seen that the output driver transistors are connected to a separate power pad, VCC2. The advantage of the separation of power supplies is to avoid the problem of high output currents coupling to the input circuitry. In addition, VCC2 can be independently adjusted. Lower VCC2 can also decrease power dissipation, but normally it should not be more than 2.0 volts lower than VCC1.

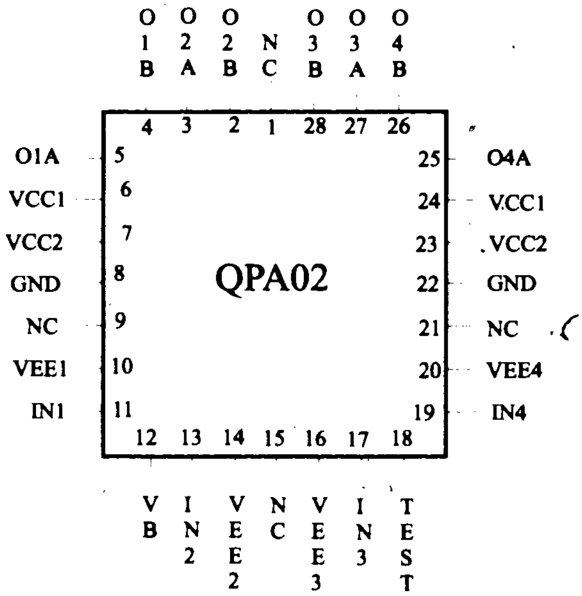

Figure A1.2 Pad diagram of QPA02 chip

QPA02 chips bonded into 28 pads chip carrier are available, which contains four amplifiers. The pad diagram is shown in Figure A1.2. Power supply pads and ground pads are on either side. The input stages are on the bottom half of the chip, and the amplifier stages are on the top half, which maximizes isolation between inputs and outputs. A separate reference pad (VEE) is necessary for each channel to avoid common impedance crosstalk. Since this amplifier has a large gain-bandwidth, special care in grounding and shielding is required for practical use.

Appendix 2 Microgap Chamber Prints

Microgap Chamber (MGC), proposed by Angelini [23] in 1993, is a modified MSGC detector to avoid charging up of the insulating substrate. In this thesis, we attempted to fabricate microgap chamber detector prints with the existing techniques in the cleanroom laboratory, Simon Fraser University. Two approaches were presented to fabricate the MGC prints in this chapter: spin-on-glass insulating layer and anisotropic etching method.

The instrintic feature of MGC detector is that the separation between anode and cathode is only a few microns, therefore the collecting time of avalanche charge is very short. Another advantage of MGC over MSGC is that the charge accumulation problem can be avoided in MGC because there are nearly no insulating materials exposed to ionization gas. MGC can also be built using microelectronics technology.

The MGC detector has been implemented with plasmas enhanced chemical vapour deposition and dry etching processes. In this thesis, some microgap prints were designed, and then fabricated with two alternative approaches. First, a spin-on-glass was used as an insulation layer. Second, a structure, which was formed with anisotropic etching process, was used in MGC prints.

A2.1 Microgap chamber print with spin-on-glass insulation layer

A2.1.1 Structure of microgap plate

Fig. A 2.1 shows the top view and cross section of the detector plate, which consists of substrate, the first metal film, insulating layer and the second metal film.

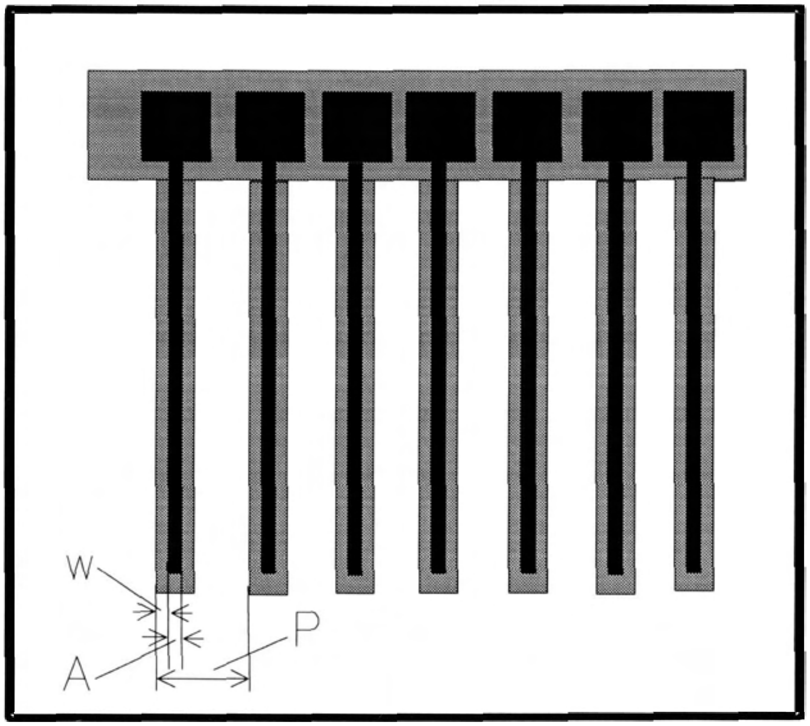

(i) top view

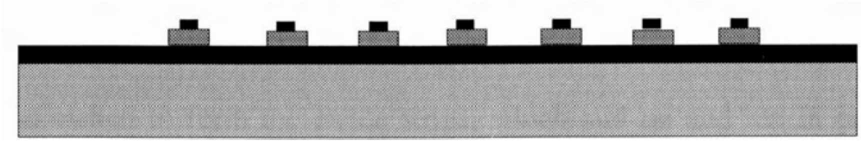

(ii) cross-section view

Figure A2.1. Structure of MGC print, (i) top view, (ii) cross section view

A - anode width (10μm), W - edge (5μm), P - anode pitch (200μm)

(a) Substrate. In our project, the *p*-type silicon wafers of <100> orientation were used as substrate, which act only as a mechanical support. Silicon wafer were used due to this uniform defect free surface, low cost, and easily handling in standard procedure with standard clean room equipment. Eight different designs were integrated on each 4 in. wafer.

(b) The first metal film. This aluminum layer of about 1 micrometer thick was deposited by sputtering process on the silicon wafer. This metal layer was used as a cathode to collect the positive charge.

(c) insulating layer. The insulating layer is formed by putting the multiple layer of spin-on-glass on the top of the first metal layer (see section 6.1.1.3). The insulating strips were obtained by patterning and etching the spin-on-glass layer with BOE (Buffered Oxide Etchant). The thickness of the spin-on-glass layer is 1.1um, 1.3um and

1.4um, respectively, where the insulating layer was 10 micro and 20 micro wider than the anodes.

(d) The second metal layer. This aluminum layer of about 1 micrometer thick was deposited by sputtering process on the top of the spin-on-glass. This aluminum layer was patterned and etched to form the anode strips, which laid on and ran in parallel to the oxide microstrip beneath. The width of the anode strips were 20, 30, 40 and 50 microns, respectively. There were two lengths of the anodes, 14.9um and 37um.

A2.1.2 Print fabrication process

The process of fabrication of the microgap prints can be divided into two steps, i.e. film depositions and etching.

(a) Film deposition.

In the fabrication of the microgap plate, we need to deposit aluminum film twice by sputtering as well as to deposit the multiple layer of spin-on-glass between the two metal layers. Before the deposition of the first metal layer, the surface of silicon wafer is prepared with RCA cleaning process, which includes the removal of organic material, silicon oxide and metallic ion. Both of those two aluminum layers were deposited in the ambient of argon at the pressure around 10^{-3} torr. The thickness of aluminum layers were controlled by power and timing to about 1 micrometer.

For the insulating layer, we used the ACCUGLASS 311 spin-on-glass to form silicon oxide film on the top of the first metal layer. The ACCUGLASS 311 spin-on-glass is a product of Allied Signal Corp., which is the widely used planarization material in IC industry. The relationship between spin speed and final thickness is :

$$z \propto \frac{1}{\sqrt{\omega}} \qquad \text{(A2.1)}$$

where the z is the final thickness and ω is the spin speed. From the data sheet we know that, the ACCUGLASS 311 spin-on-glass will yield film thickness of 3200Å when spinning at 3000 r.p.m.. We also measured the thickness of a spin-on-glass layer formed with spinning at 2000r.p.m. with profile meter. It is about 3800Å. With Equation (A2.1), the thickness of spin-on-glass can be estimated, as listed in table A2.1.

In our experiments, we deposited three samples with different spin-on-glass layers. For the first one, three spin-on glass layers were coated sequentially on the surface of the first aluminum film, in which the spinning speed for the first two layers is 2000 rpm and then the spinning speed increase to 3000 rpm for the third layer. The thickness of the isolating layer is about 10700Å (1.07μm). The second sample was coated with three layers by 2000 rpm and one by 3000 rpm, so the thickness can be estimated as 14500Å (1.45μm). The reason that we used high spinning speed at the final layer is to obtain a smooth surface for deposition of the second aluminum film. Obviously, that smooth surface is especially important here because a intensive electric field will be built up between the anodes and the cathode for avalanche amplification. A coarse surface will cause discharge at relatively low voltage.

table A2.1. Estimated film thickness at different spinning speeds

spin speed (rpm)	3000	2000	1000	500
thickness (Å)	3102	3800	5374	7600

For testing, we also try to coat the spin-on-glass layer with low spinning speed. The third sample was coated with two layers of spin-on-glass by 500 rpm. The corresponding thickness of the isolating layer is about 15200Å (1.52μm). The specification of those insulating layers are summarized in table A2.2.

Table A2.2. specification of the insulating layers

	sample 1	sample 2	sample 3
configuration	2×(2000)+1×(3000)	3×(2000)+1×(3000)	2×(500)
thickness	1.07μm	1.45μm	1.52μm

The number in ( ) stands for spinning speed

Thickness is estimated with Eq (1)

It should be pointed out that the deposition of spin-on-glass usually includes a triple hot plate bake sequence (100°C, 200°C, 400°C) after each spin coat. The hot plate bake configuration starts with a low temperature hot plate and increases with successive plates. These sequential temperature increases allow gradual solvent evaporation. A low initial hot plate temperature can also improve planarization and lower defects. For multiple coats, the temperature of the hottest plate should be sufficiently crosslink the film so that it is not dissolved by the solvent of subsequent dispenses.

(b) etching.

The conventional isotropic wet etching processes were used here to pattern the second metal and insulating layers. For the second aluminum layer, the etching process is operated at the temperature about 50°C with the aluminum etchant. The spin-on-glass layer was etched by BOE. Caution must be taken in the etching process of insulating layer because the etchant of BOE also etch the first aluminum layer. Fortunately, the etching speeds of BOE to spin-on-glass and aluminum layer are quite different. Before fabrication, we tested the etching processes of spin-on-glass and aluminum layer separately. It was found that it would take about 30 seconds and 10 minutes to remove the spin-on-glass and aluminum layer of 1μm thick, respectively. So, we can control the etching process of spin-on-glass layer by timing.

The detailed operating conditions used in etching processes for metal layer and insulting layer are listed in table A2.3. This is a multiple layer etching process, so the alignment was necessary.

table A2.3. etching conditions for metal and insulating layers

	aluminum layer	spin-on-glass layer
exposure time (sec)	23	30
etchant	aluminum etchant	BOE
etching temperature (°C)	50	room temperature
etching time (sec)	120	30

For those three samples, we used the same mask for the second metal layer and different masks for the insulating layer so that the configuration parameters indicated in Fig.6.1 of each prints as the following:

table A2.4. configuration parameters of microgap prints

	sample 1	sample 2	sample3
A (μm)	20, 30, 40, 50	20, 30, 40, 50	20, 30, 40, 50
anode thickness (μm)	1.1791	1.1772	1.1811
anode pitch (μm)	200	200	200
W (μm)	0	10	20
SOG thickness (μm)	1.0105	1.2977	1.4515

SOG: spin-on-glass

For sample 1, SOG thickness is estimated by using the average of sample 2 and 3 as anode thickness of

We also measured the aluminum and spin-on-glass layers with profile meter. The measured results are also listed in table 6.4, which agree very well with the estimated values above.

A2.2 Microgap print by anisotropic etching processing

The microgap structure were fabricated on the silicon wafer, and an anisotropic etching technique was used to form the microgap structure. Being compared with previous MGC structures, the new fabrication procedure is only involve the photolithography process once. So, any defects caused by misalignment during multilayer procedure were avoided in the new method.

A2.2.1 New approach to MGC structure

A new approach to MGC structure was proposed, in which the microgap structure was formed on silicon wafer first, then a metal layer is deposited on the top of this structure to form anode and cathode. The procedure is shown in Figure A2.3.

The microgap structure can be realized through anisotropic etching process. By using ethylene diamine, pyrocatechol and water (EDP) as etchant, the anisotropic etching rate ratio between (100) and (111) direction of silicon crystal is about 35:1. Therefore, with the anisotropic etching process some unique geometry may be realized with silicon wafer. Figure A2.3(a) shows the cross section view of grave formed by the anisotropic etching on (100) wafer. The angle of the side wall is about 54.74°, which is angle between the <100> plane and <111> plane.

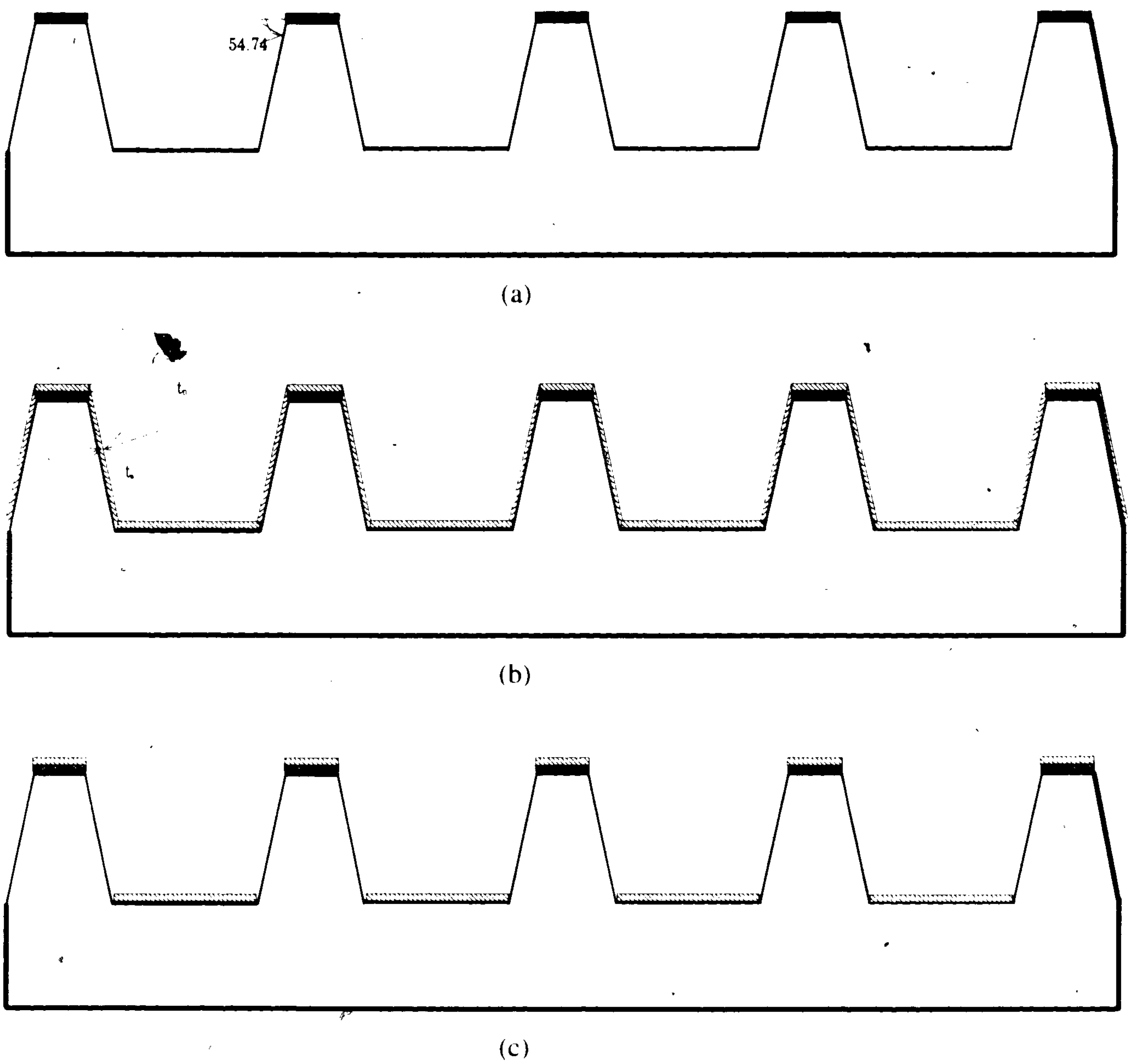

Figure A2.3 Schematic of MGC print fabrication on silicon wafer. (a) microgap structure formed by EDP etching on (100) silicon wafer; (b) aluminum film deposition on top of micro structure; (c) MGC print after removing aluminum film on side wall.

A metal layer is deposited on the top of microgap structure by DC sputtering, as shown in Figure A2.3(b). Since the sputtered metal particles is deposited perpendicular to the surface of substrate, metal film on sidewall will be thinner than that on the other area. The thickness of the side wall film can be estimated with:

$$t_s = t_0 \cdot \cos\vartheta = 0.577 t_0 \qquad \text{(A2.2)}$$

where t_s and t_0 are the thickness of metal film on side wall and other area, respectively. The thickness difference between the side wall film and others enable us to remove the metal film on the side wall area by controlling the conventional metal etching process. The residual metal films on the top and bottom will works as anode and cathode, respectively.

The advantage of this new approach is that only one photolithography process is used in fabrication. For the previous MGC process, multiple photolithography is involved to pattern both the second metal layer and the insulating layer. The alignment between each patterning is crucial because a very high voltage will be applied between the anode and cathode for avalanche amplification. The error tolerance of the alignment becomes stringent when fabricating large area x-ray detector of MGC. Since only one etching process is used in our fabrication, the deliberate mask alignment is avoided. Also, the thermally grown oxide has a higher break down voltage than the spin on glass.

A2.2.2. Fabrication Process

The process of fabrication of the microgap prints can be divided into two steps, i.e. microgap structure formation and electrodes deposition.

(a) Microgap structure formation

Microgap structure was fabricated on (100) silicon wafer by anisotropic etching technique with EDP. The reasons that EDP was used as etchant are: (1) a large anisotropic ratio (35:1) is possible with EDP; (2) it can be masked by SiO_2 and many other materials. In this project, microgap structures were fabricated on four silicon wafers. We also used SiO_2 layer as the mask for EDP etching. The fabrication process includes the following steps:

- *Oxidation of silicon wafer*

The silicon oxidation of those wafers was done in steam at about 1100°C for about 45 min. The thickness of the oxidation layer is about 0.5μm, which can be estimated by color of the film.

- *Oxidation patterning*

The oxidation layer was patterned with the mask. The patterned oxidation was used as mask in the following EDP etching process.

- *EDP etching*

Anisotropic etching processes of patterned silicon wafers were conducted with EDP etchant. The temperature of EDP solution was about 96°C. Different etching period was used to each wafer for different depth of microgap structure. The grave depth of microgap structure was measured with profilometer. The etching time and resultant microgap depth were listed in table 6.5.

Table A2.5 EDP etching and measurement results

	temperature (°C)	time (min)	depth (μm)
Wafer A	96	7	3.7069
Wafer B	96	15	13.8437
Wafer C	96	25	23.4814
Wafer D	96	50	~46

Limited by the measurement range (30μm) of profilometer, the depth for Wafer D can not be measured.

(b) Electrode deposition

The electrodes (both anode and cathode) are made from the aluminum film deposited by sputtering. Then the aluminum layer was etched without mask. Since the thickness of aluminum layer was different on the side wall and other places, the aluminum film on side wall would be removed first. The etching process was stopped at this moment, and the residual aluminum films on top and bottom of the grave were used as anode and cathode, respectively. In the aluminum film deposition of wafer A and C, a DC biasing voltage was applied between the substrates and aluminum target. The purpose of this DC biasing is to accelerate aluminum particles in sputtering and improve the collimate the particle beam. It was expected that this measure can ensure the film thickness difference between the side wall area and others. A biasing voltage of 200 volts was used, which is limited by the specification of sputtering machine. For comparison, aluminum was deposited on wafer B and D without DC bias.

Sputtering was conducted in the Ar ambient of 10^{-6} Torr. The sputtering process is controled by current, and thickness of the aluminum film was around 1μm.

(c)Aluminum etching

After deposition, the aluminum was etched with aluminum etchant. From eq. (1) it can be found that the thickness of aluminum layer on the side wall is about 0.577μm while thickness of aluminum on other area is about 1μm. After etching, about 0.3μm aluminum was left, this was used as anode or cathode.

Timing in this etching process was critical. The aluminum etching was conducted in room temperature instead of 50°C to slow down the etching rate for control ease. The etching process was stopped from time to time, and resistance between anode and cathode was measured with a multimeter. The whole etching process was finished when it was found that resistance between anode and cathode became infinite.